1

Lithium Metal Batteries

1.1 History

Li metal has been widely regarded as the ideal anode material due to its ultrahigh theoretical specific capacity (3860 mAh g^{-1}) and very low redox potential (~3.040 V vs. standard hydrogen electrode) [1, 2]. The first visible Li metal secondary battery was operated by Stanley Whittingham at Exxon in the 1970s. In the late 1980s, Li metal batteries based on MoS_2 cathode and excess Li were commercialized and sold to the market, which could be cycled hundreds of times. But due to safety accidents, including fires caused by Li dendrites, all the cells were recalled [3]. Since then, safety concerns about Li metal anodes still prevail. Although NEC and Mitsui realized an ultra-long cycling stability of Li metal cells over 500 000 cycles, the safety issue is not solved. Later, Sony Company developed a safe Li-ion battery based on a carbonaceous anode instead of Li metal, which can overcome the safety concerns related to Li dendrites, and these kinds of cells were commercialized and are in use until today [4]. As a result, the studies on Li metal anodes were halted.

Now, with the emergence of vehicle devices and hybrid grids, the state-of-the-art Li ion batteries based on graphite anodes are reaching their theoretical capacity, which cannot fulfill the increasing demand for high energy density [5]. Therefore, the application of Li metal as anode attracts the researchers. Over the four decades of research on Li metal anodes, great achievements have been made in improving the energy density and cycling stability of Li metal batteries [6]. Among them, various cathode alternatives have been reported, such as intercalation cathodes [7], sulfur/selenium/tellurium composites [8–10], oxygen/air electrodes [11], iodine/bromine flow cathode [12], and lithium-free transition metal oxides [13]. These batteries have their own advantages, but also exhibit their intrinsic problems, which hamper practical applications of Li metal batteries. But these battery systems all have common problems related to Li metal [14]. First, Li metal can react with the electrolyte to form a solid electrolyte interphase (SEI) layer on the surface, which will consume the electrolyte and increase the internal resistance. Second, Li dendrites will grow and cause safety concerns. Third, large volume change of Li metal can break the SEI and lead to further reaction between Li metal and the electrolyte, resulting in the failure of cells. All these disadvantages need to be addressed before the commercialization of Li metal batteries.

Liquid Electrolyte Chemistry for Lithium Metal Batteries: Design, Mechanisms, Strategies,
First Edition. Jianmin Ma.

1.2 Types

In this chapter, we summarize several different types of Li metal batteries, such as lithium–oxygen batteries, lithium–sulfur batteries, lithium–selenium/tellurium batteries, lithium–iodine/bromine batteries, and lithium-free transition metal oxide Li batteries. In each section, we first introduce the working mechanisms, then the design strategies for cathode structures, the modification of electrolyte, and the protection methods for Li metal anodes.

1.2.1 Lithium–Oxygen Batteries

With the continuous consumption of nonrenewable fossil fuels and new requirements for carbon neutrality, green energy systems have been paid much attention. Among them, Li–O_2 batteries using O_2 as cathode and Li metal as anode have the highest energy density ($\sim$3500 Wh kg^{-1}). The cathode, O_2, can be inexhaustibly extracted from open air and show the lightweight property to reduce the whole weight of Li–O_2 cells. Unlike cathodes in Li–ion batteries, that consist of high-cost nickel or/and cobalt metal, the abundance and cheap O_2 cathodes can dramatically reduce the cost of Li–O_2 batteries. Moreover, the Li anode exhibits high specific capacity and lowest electrochemical potential. Although Li–O_2 batteries have so many advantages over Li–ion batteries, their practical applications are hampered by the sluggish oxygen reduction reactions (ORR) and oxygen evolution reactions (OER) and random deposition of discharge products (Li_2O_2), leading to high overpotentials, low capacity, and unstable cycling performance [15]. In this section, the working mechanism of Li–O_2 batteries is discussed first and then the reasonable design for cathode and anode protection is summarized. Finally, problems are summarized and future directions are provided.

1.2.1.1 Working Mechanism of Li–O_2 Batteries

As shown in Figure 1.1a, a Li–O_2 battery consists of three parts: Li metal anode, electrolyte, and porous cathode [16]. Unlike other energy storage systems, the Li–O_2 battery is a semi-open system, which can allow O_2 penetrate into the cathode side to participate in electrochemical reactions. During discharge, the Li anode will be oxidized to generate Li^+, and the oxygen is reduced on the cathode side, which can react with Li ions to form Li_2O_2, as described by Eq. (1.1):

$$O_2 + 2Li^+ + 2e^- \rightarrow Li_2O_2 \tag{1.1}$$

It looks very simple according to the reaction equation, but this direct reaction seems unlikely to occur electrochemically because the two-electron process requires much higher entropic barriers than that of a one-electron process. Actually, the discharging process is much more complicated than the equation [18], which is shown in Figure 1.1b. O_2 is first adsorbed on the active sites of cathode materials, donated as O_2^*, and then O_2^* will get one electron and reacts with Li^+ to form LiO_2^* (Eq. (1.2)):

$$O_2^* + Li^+ + e^- \rightarrow LiO_2^* \tag{1.2}$$

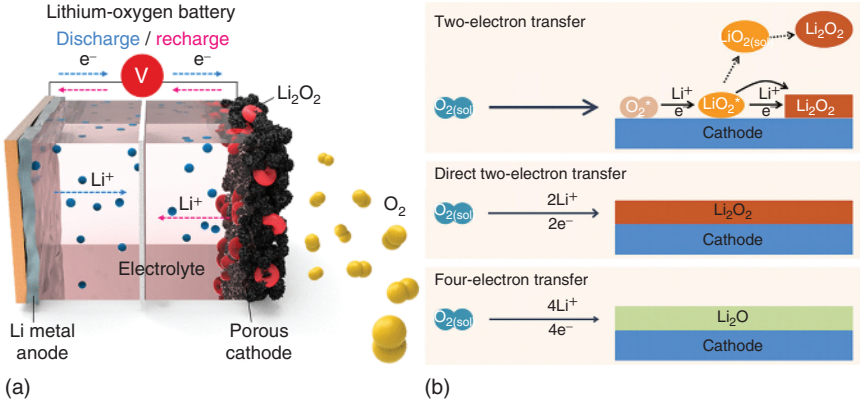

Figure 1.1 (a) Schematic operation proposed for rechargeable aprotic Li–O_2 batteries. Source: Reproduced with permission Kwak et al. [16]. (b) Schematic of the Li_2O_2 growth pathways. Source: Reproduced with permission Lyu et al. [17]. Reproduced with permission of (2017) Royal Society of Chemistry.

After that, the LiO_2^* have three possible reaction pathways to finally transfer to Li_2O_2, as described by the following equation:

$$LiO_2^* + Li^+ + e^- \rightarrow Li_2O_2^* \tag{1.3}$$

$$LiO_2^* + LiO_2^* \rightarrow Li_2O_2^* + O_2^* \tag{1.4}$$

$$LiO_{2(sol)} + LiO_{2(sol)} \rightarrow Li_2O_2 + O_2 \tag{1.5}$$

The LiO_2^* forms $Li_2O_2^*$ through electrochemical reduction (Eq. (1.3)) or disproportionation on the surface (Eq. (1.4)), both of which are referred to as the surface growth model. It has been reported that the electrochemical reduction pathway can be easily realized due to the low kinetic barrier and free energy [19]. The adsorbed LiO_2^* may also diffuse into the solution by modulating the electrolyte, which can be converted into Li_2O_2 via disproportionation in solution (Eq. (1.5)), which is regarded as the solution growth model.

The most expected is the four-electron transfer process, i.e. the O_2 is fully reduced to lithium oxide (Li_2O) because of its higher electron transfer number. However, this reaction pathway is kinetically impossible because Li_2O is not observed by any spectroscopic technique at a cutoff voltage of above 2.0 V. Moreover, during the charging process, the Li_2O could not convert into O_2 [20]. On the cathode side, carbonaceous materials as matrixes can be decomposed on high voltage or react with Li_2O_2 to form Li_2CO_3 [21]. These solid side products will accumulate on the cathode surface, leading to blockage of electron and O_2 channels and the failure of battery. Therefore, cathode materials with suitable pore and relatively high pore volume are desirable. The superoxide as discharge product can react with the electrolyte and form side products on the cathode surface. In addition, due to the intrinsic sluggish ORR/OER process, the rate capability of Li–O_2 batteries is poor and catalysts should be applied on the cathode side [22, 23]. In view of

semi-open property of Li–O_2 batteries, Li metal anodes are unstable with O_2 and H_2O, leading to gas generation and corrosion of Li anode. Thus, long-term stable Li–O_2 batteries will not be realized until proper strategies are made for cathode structure design, electrolyte modification, and Li anode protection. From this discussion, we conclude that even Li–O_2 batteries can provide high energy density, the challenges still exist on the way to make them applicable.

1.2.1.2 Cathode Design of Li–O_2 Batteries

The structures and morphologies of cathode materials in Li–O_2 batteries directly affect the ORR and OER activities, thus determining the energy density and coulombic efficiency of Li–O_2 batteries. The commonly used cathodes are based on carbon materials due to their high conductivity, high surface area, low cost, lightweight property, and various and controllable structures [24]. The ideal cathode structure should have high chemical/electrochemical stability in the reversible cycling process; high surface area with mesoscale pores for large Li_2O_2 storage, suitable porosity to control the size of Li_2O_2 product; and high electrical conductivity to reduce the overpotential caused by the insulator and insoluble Li_2O_2 product.

For the cathode design, at the beginning, researchers largely focused on preparing nanosized materials with high conductivity and high surface area. For example, Zhang's group reported a porous air electrode with functionalized graphene sheets (FGSs) with lattice defects and hydroxyl, epoxy, and carboxyl groups (Figure 1.2a) [25]. The prepared FGSs consist of interconnected bimodal pore structures with micro- and nanometer length scales, which facilitate the penetration of O_2 and the transportation of electrons. In addition, the density functional theory (DFT) calculation indicates that the lattice defect sites on the FGSs can help to form small, nanometer-sized discharge products (Li_2O_2). The FGS-based air cathode (with no catalyst) delivers an exceptionally high capacity of 15 000 mAh g^{-1}. In 2016, RuO_2/CNT (carbon nanotube) was synthesized as cathode for Li–O_2 batteries by Zhang's group. Due to the synergistic effect of RuO_2 with good catalysis and CNT with high conductivity and 1D structure, the battery delivered a high discharge capacity of 29 900 mAh g^{-1} and a relatively long cycling stability over 171 cycles. Recently, Sun's group fabricated porous Mo_2C/C nanoflowers assembled by ultrathin carbon nanosheets decorated with Mo_2C quantum dots (Figure 1.2b,c) [26]. As cathode materials, Mo_2C/C materials show excellent catalytic activity with a low discharge/charge gap of 1.2 V in the first cycle (Figure 1.2d). The ultrathin carbon nanosheets could suppress the agglomeration of Mo_2C quantum dots, as well as improve the conductivity of the Mo_2C/C cathode. In addition, the ultrathin carbon nanosheets and porous nanoflowers structure could ensure fast Li ions and O_2 diffusion. The Mo_2C/C delivers a relatively high specific capacity of 7500 mAh g^{-1}. With a cutoff capacity of 500 mAh g^{-1}, the Li–O_2 battery exhibits no obvious capacity fading for 100 cycles (Figure 1.2e). The excellent performance may be ascribed to the synergistic effect of ultrathin carbon nanosheets, highly dispersed Mo_2C quantum dots, and the special porous structure.

But in this period, some binders were used in the preparation of cathodes, which were unstable and could be decomposed during cycling. Therefore, freestanding

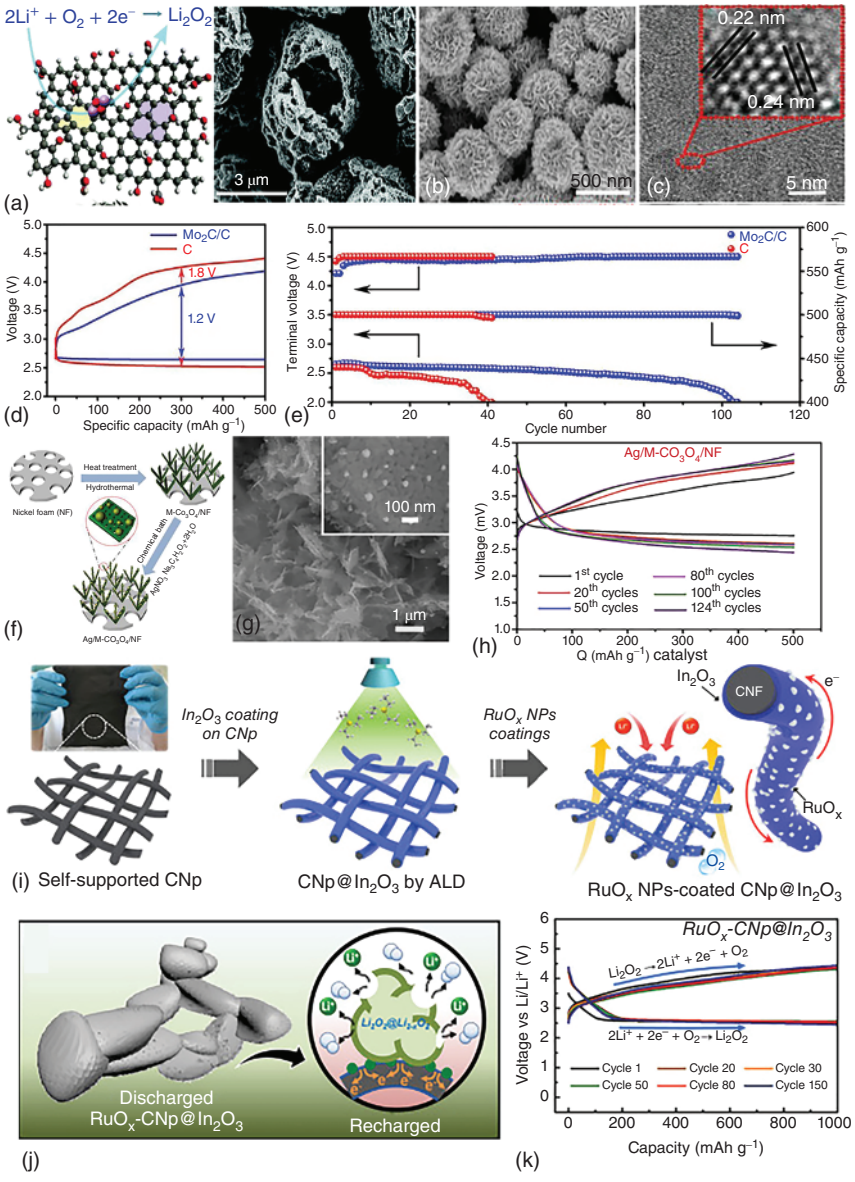

Figure 1.2 (a) Schematic structure of a functionalized graphene sheet with an ideal bimodal porous structure. Source: Xiao et al. [25] / with permission of American Chemical Society (b) SEM and (c) TEM images of Mo_2C/C. (d) The first discharge/charge curves and (e) cycling performance of Mo_2C/C and C as cathodes at 100 mA g^{-1}. Source: Jiao et al. [26] / with permission of Elsevier. (f) Synthetic procedure of Ag/M-Co_3O_4/NF composite structure; (g) SEM image of Ag/M-Co_3O_4/NF composite; (h) discharge/charge curves of Li–O_2 batteries with Ag/M-Co_3O_4/NF electrode at different cycles. Source: Huang et al. [27] / with permission of Elsevier. (i) Schematic illustration of synthesis of RuO_x-CNp@In_2O_3; (j) suggested illustration for Li_2O_2 decomposition in RuO_x-CNp@In_2O_3; (k) Discharge–charge profiles of RuO_x-CNp@In_2O_3 at a current density of 0.2 mA cm^{-2} with a fixed capacity of 1000 mAh g^{-1}. Source: Jung et al. [28] / with permission of Elsevier.

and binder-free cathodes were developed using simple hydrothermal or chemical vapor deposition methods. Various freestanding morphologies with catalysts were reported, such as nanoarrays, nanowalls, nanowires, grown on carbon paper or nickel foam or carbon cloth [29–31]. In 2017, Luo and coworkers prepared Ag-decorated highly mesoporous Co_3O_4 nanosheets on nickel foam using the hydrothermal and chemical bath method (Figure 1.2f) [27], which were used as freestanding cathodes for Li–O_2 batteries. Ag nanoparticles can improve electrical conductivity of the O_2 electrode and provide a catalytic activity for ORR. Mesoporous Co_3O_4 nanosheets with a thickness of 10 nm are beneficial to accommodating insoluble discharge products and facilitating oxygen diffusion and electrolyte impregnation (Figure 1.2g). Due to the synergistic effect, Ag/M-Co_3O_4/NF exhibited a robust catalytic activity, delivering a high reversible capacity of 2471.1 mAh g^{-1}, a low discharge/charge overpotential, and a cycle life over 124 cycles (Figure 1.2h). The RuO_x functionalized In_2O_3 coated freestanding carbon paper was designed by Kim and coworkers (Figure 1.2i) [28]; the In_2O_3 is unreactive to superoxides and can prevent direct contact between the carbon paper and the Li_2O_2 to generate parasitic side products such as Li_2CO_3 (Figure 1.2j). The catalytic RuO_x leads to a significant reduction in the overpotential (Figure 1.2k), acting as an electron transfer bridge between the Li_2O_2 and In_2O_3 layer. Thus, the cycling stability of Li–O_2 batteries can be extended to 165 cycles. For the aforementioned cathodes, either nickel foams or carbon paper/cloths with a diameter over 10 μm are used as the current collector, which has low surface area and limits the contribution to capacity. To increase the surface area, freestanding nanofibers with small diameters and rich active sites were prepared by the electrospinning method. Freestanding activated carbon nanofibers (ACNF) were prepared through electrospinning combined with CO_2 activation by Zhang's group [32]. The loosely packed nanofibers can improve the permeability of O_2 across the cathode. The mesopores introduced by CO_2 activation act as additional nucleation sites for Li_2O_2 deposition, leading to reduced size and flake-like individual Li_2O_2 particles.

Apart from the carbon-based cathodes, carbon-free cathodes have been investigated because of their chemical stability [33]. Carbon materials can react with superoxides to produce Li_2CO_3, exhibiting unstable properties. Carbon-free cathodes can prevent this side reaction to improve the stability of cathodes in a long cycling process. A yolk–shell catalyst of Co_3O_4@$NiCo_2O_4$ was prepared using ZIF-8@ZIF-67 materials as the template and then coating with $NiCo_2O_4$ (Figure 1.3a) [34]. Co_3O_4@$NiCo_2O_4$ composite exhibited excellent ORR and OER performance due to the adjustable structure, abundant active sites and open space (Figure 1.3b), delivering a high discharge capacity of 11 672.8 mAh g^{-1} and a long cycle life of 280 cycles. Compared with metal oxides, all metal-based matrixes have received much attention because of their high conductivity. Recently, Xu and coworkers nanoengineered Au-coated Cu nanoneedle arrays grown directly on a Cu foam structure (Au/Cu@FCu) as both the anode backbone and the cathode in a Li–O_2 battery [35]. Due to their excellent conductivity, high porosity, large specific surface, and superior lithiophilicity as well as high catalytic activity, Au/Cu@FCu electrodes can simultaneously regulate uniform deposition of lithium metal on

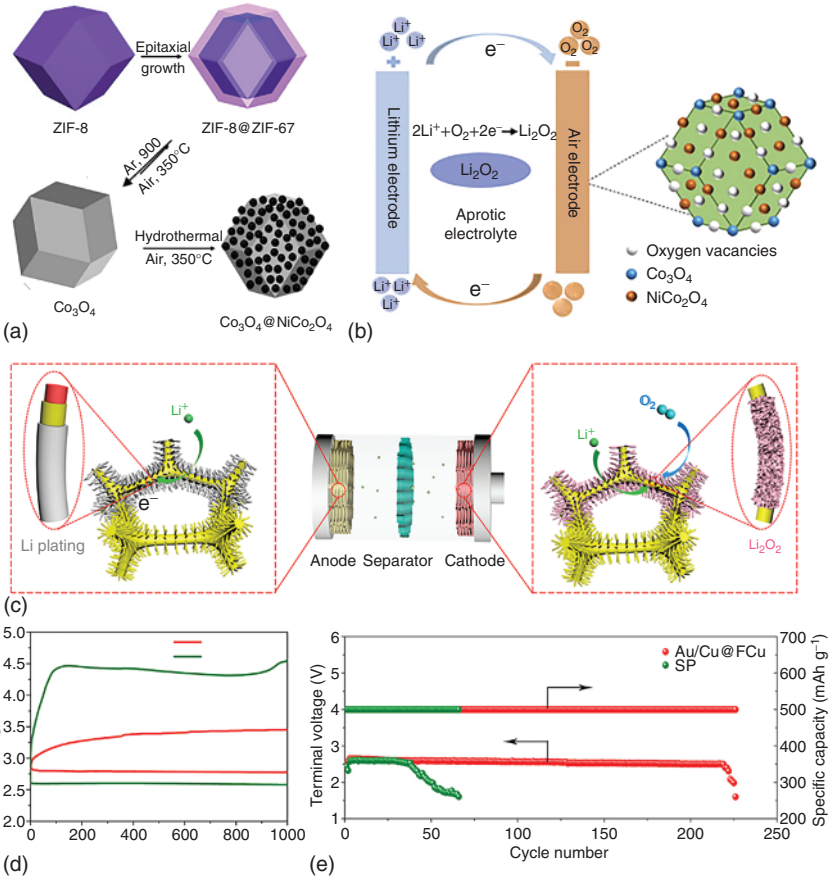

Figure 1.3 (a) Preparation of Co_3O_4@$NiCo_2O_4$; (b) electrochemical mechanism of the cells with Co_3O_4@$NiCo_2O_4$ as catalyst. Source: Reproduced with permission Zhao et al. [34]. (c) Synthetic mechanism of Au/Cu@FCu for the symmetrical Li–O_2 battery; (d) first discharge–charge voltage profiles of the Li–O_2 battery with the SP cathode and Au/Cu@FCu cathode at a current rate of 100 mA g^{-1} with a limited capacity of 1000 mAh g^{-1}. (e) Discharge terminal voltage vs. cycle number for two different cathodes with 100 mA g^{-1} at a fixed capacity of 500 mAh g^{-1}. Source: Reproduced with permission Luo et al. [35].

the anode and catalyze the formation/decomposition of Li_2O_2 on the cathode (Figure 1.3c). As a result, the Au/Cu@FCu cathode demonstrated extremely low overpotentials (0.64 V) (Figure 1.3d) and a very stable cycling stability over 220 cycles with 100 mA g^{-1} at a fixed capacity of 500 mA g^{-1-1} (Figure 1.3e). However, until now, the number of reported metal-based cathodes is less than that of other metal oxides or carbonaceous cathode materials due to their relatively low surface area and high mass density. Thus, designing suitable nanostructured metals is vital to improve their application.

Based on the preceding discussion, we know that materials with various structures and components have been adopted in Li–O_2 batteries. However, in some

cases, complex cathode structures do not necessarily lead to better performance. The structure of cathodes and how cathodes influence the discharge and charge processes should be investigated in coordination with electrolytes. Moreover, porous structures are synthesized by complicated procedures, which bring high costs. Developing simple ways for constructing effective cathodes is important.

1.2.1.3 Anode Protection of Li–O_2 Batteries

The Li metal in Li–O_2 batteries can be converted into LiOH during cycling caused by the reaction of Li with H_2O formed through the decomposition of electrolyte, which was discovered by Liu and coworkers through spatially and temporally resolved synchrotron X-ray diffraction and a three-dimensional micro-tomography technique [36]. In addition, there are many microscopic "tunnels" in the LiOH thick layer, which provides channels for Li ions. Since then, researchers have been paying much attention on the anode protection in Li–O_2 batteries. Based on the research results, protection strategies can be classified into artificial surface coating, electrolyte additives, and conductive matrixes to host Li metal [37].

Artificial surface coating*:* An artificial protective film on Li metal can be achieved through the reaction of Li metal with solvents via chemical or electrochemical methods. When the symmetric Li battery charging in the electrolyte consisting of fluoroethylene carbonate (FEC) solvent, a LiF-rich film on Li surface can be obtained due to the decomposition of FEC [38]. The LiF-rich SEI layer can extend the cycling stability of the Li anode from 40 to 100 cycles, because LiF could facilitate the diffusion of Li ions. Zhang's group reported a multifunctional and gradient protection layer on Li metal through the reaction between molten Li with poly(tetrafluoroethylene) (PTFE), resulting in a LiF/F-doped carbon-gradient protection layer (Figure 1.4a) [39]. The rich polar C—F bonds on the surface could uniformly capture Li ions and regulate the electron configuration of LiF to make Li ions quasi-spontaneously diffuse from carbon to LiF surface. The LiF at the bottom could make fast Li ions transportation and homogenize the nucleation sites on lithium. As a result, this well-designed gradient protection layer offers dendrite-free Li metal anodes during cycling process in both ether-based and carbonate ester-based electrolytes [39]. Recently, molecular layer deposition was also reported by Adair to form a protective zircon layer on Li metal, resulting in a long life of 500 cycles in Li–O_2 batteries (Figure 1.4b) [40]. The artificial SEI layer via electrochemical or chemical methods are nanoscaled irrespective of thickness or structures, which may be destroyed during the long cycling process. To improve the stability, thick and mechanically stable films need to be designed on Li metal. Luo and coworkers designed a thick SiO_2/GO (graphene oxide) hybrid film (~22.0 μm) on Li metal surface (Figure 1.4c) [41]. The GO sheets act as a barrier to prevent the attack from oxygen species and moisture and suppress the growth of Li dendrites; the SiO_2 nanoparticles embedded on the GO sheets can effectively inhibit the agglomeration of GO sheets, as well as provide rich channels for Li ion transportation. The Li–O_2 battery with thick SiO_2/GO film-protected Li anode can stably cycle for 348 times with a capacity

of 1000 mAh g^{-1}. Although artificial surface coating can obtain good cycling stability and effectively suppress the dendrite growth, the coating layer normally could increase the interfacial resistance of Li–O_2 batteries, leading to high overpotentials and fading of cycling performance.

Electrolyte additives: Exploring suitable electrolyte additives to in situ form a functional SEI protective layer during cycling process is also regarded as a promising strategy [44]. Fox example, Zhang's group added tetraethyl orthosilicate (TEOS) into the electrolyte [42]. TEOS can spontaneously react with the main lithium corrosion product (LiOH) to form a Si-O-containing film on the lithium metal anode and provide a dynamic self-healing effect. This film could effectively prevent lithium from further corrosion by O_2, H_2O, and discharge intermediates in the electrolyte (Figure 1.4d). Grey and coworkers added LiI into the electrolyte of Li–O_2 batteries with porous rGO as cathode [43]. Due to the presence of LiI, the Li–O_2 battery operation involves the reversible formation and removal of LiOH crystals instead of Li_2O_2 (Figure 1.4e), which can tolerate large quantities of water. Recently, Zhang's group developed a solid-like electrolyte by adding hydrophobic silica into the electrolyte [45]. Due to the electrostatic interaction between $CF_3SO_3^-$ and silica particles, viscosity of the optimized electrolyte was increased by 980-fold; thus diffusion of H_2O or other contaminants was much slower, which can protect the Li metal anode. The Li anode in this Li–O_2 battery achieved a long life of 550 cycles.

High-concentration electrolytes: High-concentration electrolytes (HCEs) were also studied to protect Li metal anodes through changing the solvation structure of Li ions and optimizing the contents or structures of the SEI layer. Regulating the species and concentration of salts in electrolytes can optimize the Li^+ solvation structure and adjust the SEI film to strengthen Li anode. Zhang's group adopted three salt concentrations of LiTFSI/DME (1,2-dimethoxyethane) electrolyte (1, 2, and 3 M) in Li–O_2 batteries [46]. The HCE (3 M) can lead to well-protected Li metal anode and air electrode, resulting in high capacity and stability, because the HCE can enhance the stability of electrolyte against reduced oxygen intermediates.

Metal alloys: Metal alloys instead of pure Li metal were also applied to suppress the growth of Li dendrites, such as Li/Si [47] and Li/Al [48]. But the energy density is undermined because exotic metals cannot deliver energy. Moreover, the alloying procedure is tedious and complicated.

In this section, the reaction mechanism and strategies for cathode design and anode protection of Li–O_2 batteries are discussed. Although some challenges have been successfully resolved in the past decade with various approaches, to further promote the development of Li–O_2 batteries, great efforts should be made, and several directions are provided. The mechanism of Li_2O_2 decomposition on a cathode catalyst is complicated and needs intensive investigations, especially for finding effective cathode materials with high OER catalytic activity. For practical applications of Li–O_2 batteries, the effect of CO_2 in air should be considered, which can react with Li_2O_2 to produce Li_2CO_3. In addition, as the decomposition potential of

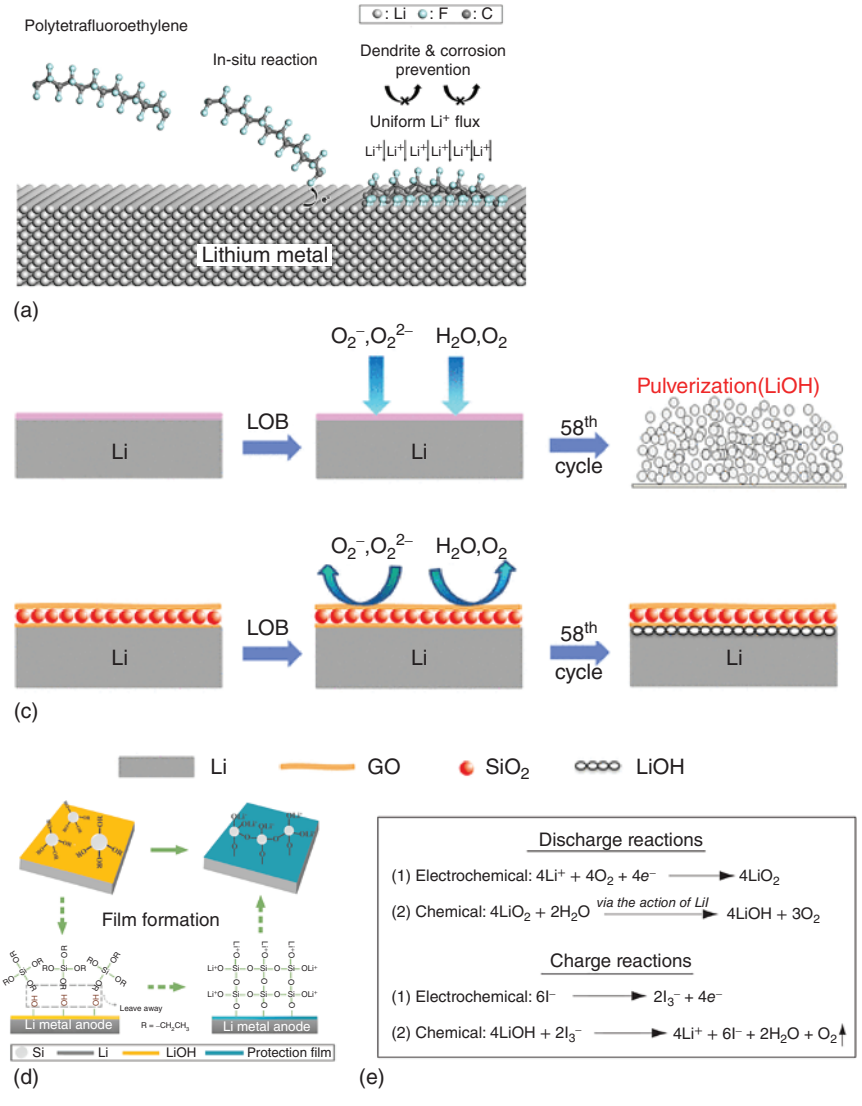

Figure 1.4 (a) Schematic illustration of the design guideline of PTL. Source: Reproduced with permission Yu et al. [39]. (b) Illustration of a protective zircon coating on a Li metal anode. Source: Reproduced with permission Adair et al. [40]. (c) Schematic illustration of mechanisms of SiO_2/GO hybrid thin layer for uniform Li deposition. Source: Luo et al. [41]. Licensed under CC BY 4.0. (d) Schematic illustration of the lithium protection film formation mechanism on TAL in Li–O_2 batteries. Source: Reproduced with permission Yu et al. [42]. (e) Schematic illustration of mechanisms for the formation and removal of LiOH in iodide redox-mediated Li–O_2 cells in the presence of water. Source: Reproduced with permission Liu et al. [43].

Li_2O_2 and Li_2CO_3 is high, it is necessary to find catalysts to decompose them at a low potential (<3.5 V). Another problem is related to the Li metal anode, such as the growth of Li dendrites. Solid-state Li–O_2 batteries should be paid much more attention, such as the improvement of conductivity, the interfacial properties of electrode and electrolyte. If these challenges can be solved, Li–O_2 batteries can take great strides forward.

1.2.2 Lithium–Sulfur Batteries

Compared with the traditional Li-ion batteries based on insertion/extraction mechanism, the lithium–sulfur (Li–S) batteries (Figure 1.5a), based on the redox reaction between Li metal and S element (Figure 1.5b), are regarded as one of the most promising next-generation energy storage systems owing to their high specific capacity (1675 mAh g^{-1}) and energy density (2600 Wh kg^{-1}), as well as the abundance of sulfur on the earth [49, 50]. Nevertheless, practical applications of Li–S batteries are hindered by intrinsic problems such as the insulating nature of sulfur and its discharge products (Li_2S), high soluble polysulfides as intermediates

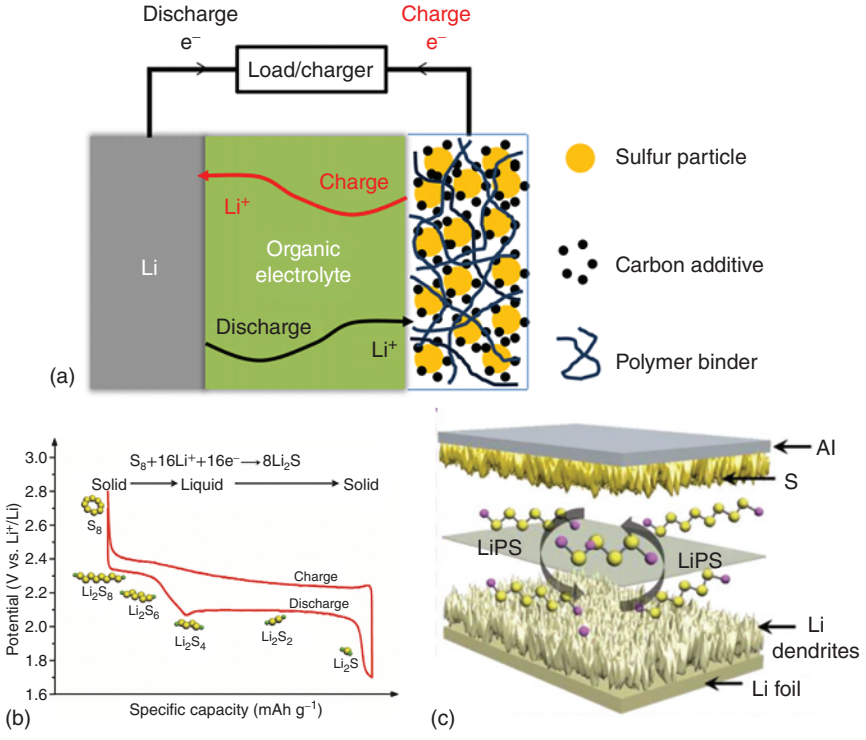

Figure 1.5 (a) Schematic diagram of a Li-S cell with its charge/discharge operations. Source: Reproduced with permission Manthiram et al. [49]. (b) A typical charge/discharge profile for a Li–S battery. Source: Reproduced with permission Ruopian et al. [50]. (c) Schematic configuration of a traditional Li-S cell. Source: Reproduced with permission He et al. [51].

during charge/discharge processes, large volume changes of electrodes, and growth of Li dendrites on the Li metal anode (Figure 1.5c) [51].

Since reported in the 1960s [52], Li–S did not get much attention due to the unclear reaction mechanism of sulfur in different electrolytes [53–55], until the cathode of sulfur embedded into a polyacrylonitrile (PAN) matrix was designed in a carbonate-based electrolyte in 2002, which delivered a relatively high and stable cycling performance (above 600 mAh g^{-1} after 50 cycles) [56]. Especially, in the past two decades, flourishing developments have been made in Li–S batteries to further enhance their electrochemical performance to promote their commercial application, including designing numerous conductive matrixes for S, introducing catalysts to promote the conversion kinetics, modifying separators to suppress the shuttle effect, exploring suitable electrolytes, and inhibiting Li dendrites. As so far, considering many review papers focused on sulfur cathode [57, 58], separators [59], and electrolytes [60] have been published, in this chapter, we mainly outline the initial and key achievements for the development of Li–S technology.

1.2.2.1 Conductive Matrixes for S Cathode

Carbon materials were first reported as conductive matrixes for sulfur in 1989 by E. Peled, which can increase the electron contact efficiency [61]. A major breakthrough on carbonaceous materials applied in S cathode is the mesoporous carbon (CMK-3) reported by Nazar and coworkers [62]. The CMK-3 shows uniform pore structure, high pore volume, interconnected conductive channels, and exhibit high conductivity, thus resulting in high utilization of active materials (Figure 1.6a). Furthermore, they coated a polyethylene glycol (PEG) layer on the surface of CMK-3/S cathode to further suppress the dissolution of polysulfides and improve the cycling stability of S cathode. Since then, great achievements have been made to fabricate porous carbon materials as conductive matrixes for sulfur cathodes [66, 67], including porous carbon, graphene, carbon nanotubes, and carbon nanofibers.

Recently, porous carbon materials as sulfur matrixes have received huge attention due to their unique porous structures, which usually possess different kinds of pore structures, including micropores, mesopores, and macropores, having the following advantages: (i) microporous pores with a diameter of less than 2 nm can encapsulate small S molecules; (ii) mesopores and macropores usually have large pore volume to loading high mass sulfur; (iii) high surface area to increase the intimate contact of sulfur with conductive matrixes, thus improving the conductivity of cathodes. In 2012, Wan's group designed a microporous carbon matrix with a pore size of only 0.5 nm, which can only confine small S_{2-4} molecules [63]. Therefore, the transition between S_8 to soluble polysulfides (Li_2S_n, $n = 4$–8) was prevented (Figure 1.6b), which can essentially solve the shuttle effect of polysulfides and improve the cycling stability of Li–S batteries. As a result, the as-obtained S_{2-4} small molecules confined in microporous carbon materials delivered a high specific capacity of 1670 mAh g^{-1} and a capacity of 1149 mAh g^{-1} after 200 cycles. To further take advantage of different pores, micro-/meso-/macroporous carbon materials with three kinds of pore properties were prepared by Tang and coworkers [68]. They systematically studied the effect of different pores on the electrochemical performance of sulfur cathodes

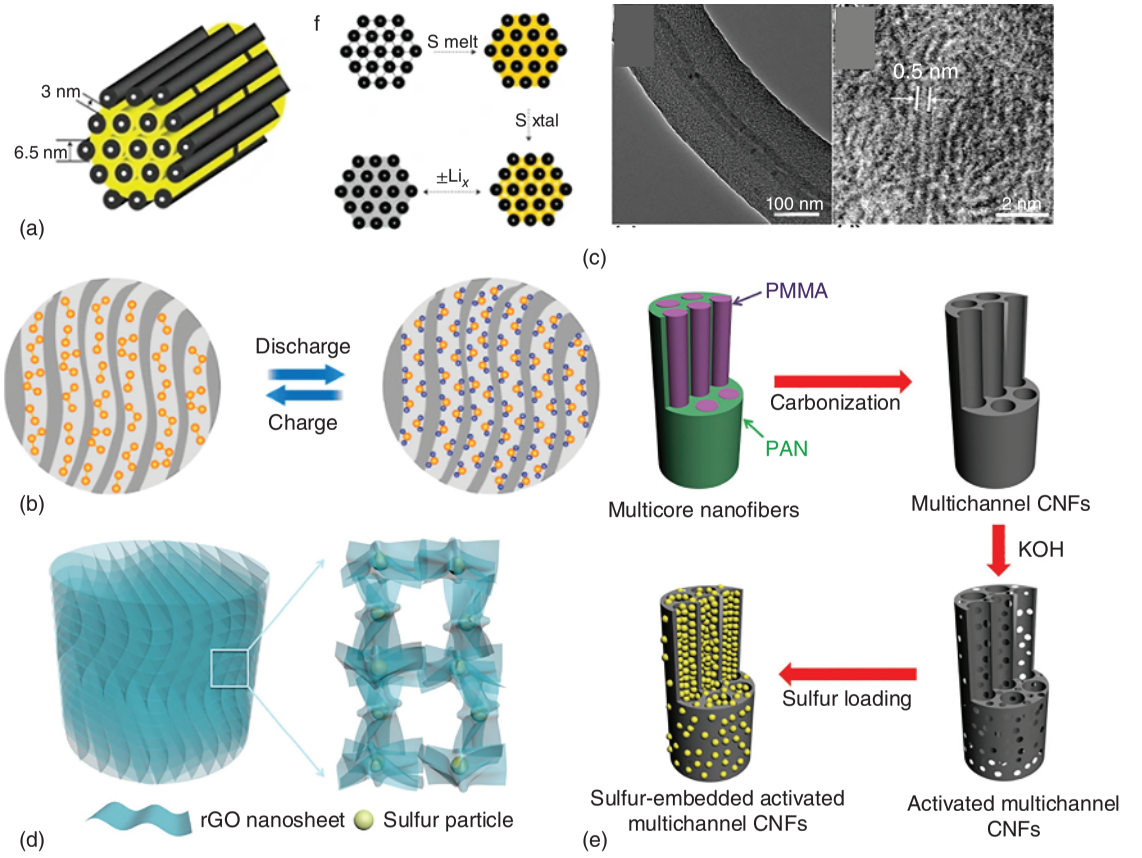

Figure 1.6 (a) A schematic diagram of S/CMK-3 composites in the discharging–charging with Li. Source: Reproduced with permission Xiulei et al. [62]. (b) Structural characterizations of CNT@MPC. (c) TEM image of a CNT@MPC nanocable. Source: Xin et al. [63] / with permission of American Chemical Society. (d) Schematic of freestanding 3D graphene/sulfur composite. Source: Reproduced with permission Papandrea et al. [64]. (e) Illustration of the sequential fabrication steps for the sulfur-embedded activated multichannel carbon nanofibers. Source: Reproduced with permission Lee et al. [65].

and reported that the pore size distribution instead of specific surface area and total pore volume influence the performance of Li–S batteries. Furthermore, the ratio of micropore volume dominates the cycling stability of S cathodes. This work will give some instructions for designing porous carbon materials for Li–S batteries.

Graphene, as a 2D carbon material, is regarded as one of the most promising conductive matrixes for sulfur due to its high conductivity, excellent mechanical property, high surface area and chemical/physical stability [69]. As the graphene freestanding film can be easily obtained, many freestanding graphene–sulfur cathodes for Li–S batteries have been reported. For example, a freestanding 3D graphene framework was prepared by Papandrea and coworkers as sulfur matrixes [64]. Due to the 3D porous structure, the mass loading of sulfur can reach as high as 90 wt%, which can greatly improve the specific capacity based on mass. In addition, the interconnected graphene walls offer many effective pathways for electron transportation and can suppress the dissolution of polysulfides into electrolyte (Figure 1.6c). Therefore, the 3D graphene/sulfur composites with 90 wt% sulfur loading could deliver a specific capacity of 341 mAh g^{-1} at 1 C after 500 cycles with a capacity retention of 77%. Carbon nanotubes and nanofibers, as other representative carbon materials, were also attracted much attention as skeletons for sulfur loading owing to their high conductivity and unique fabric structures. As a typical example, an activated multichannel carbon nanofiber (a-MCNF) was synthesized by Lee and their groups via a simple electrospinning method, followed by carbonization and KOH activation process [65]. The obtained a-MCNF materials possessed high surface area and rich micro-/mesopores. When applied as sulfur matrix, the large mesopores ensure a high sulfur mass loading (80%) and micropores help to trap soluble polysulfides (Figure 1.6d). The prepared S-a-MCNF cathode can deliver a high specific capacity of 1100 mAh g^{-1} even at a high sulfur loading of 4.6 mg cm^{-2}.

Although carbonaceous materials as sulfur host have yielded relatively stable and long cycling performance, pure carbon materials can only physically trap soluble polysulfides, which is not enough for realizing high specific capacity and long cycling stability for practical applications. Heteroatom-doped carbonaceous materials were developed because heteroatoms could strongly anchor the polysulfides through chemical bonds [70–73]. N- and O-doped carbon materials can achieve better electrochemical performance than that of other element-doped carbon materials, such as B, F, P, S, Cl, reported by Zhang's group [74]. To speed up the conversion process of soluble polysulfides, electrocatalysts were also introduced in the matrixes for sulfur [75–79], including metal oxides [80], metal sulfides [81], metal carbides [82], metal nitrides [83], metal phosphides [84], metal selenides [85] as well as single atoms [86, 87]. Apart from these metal-based catalysts, metal-free catalysts should be paid more attention, including carbon nitride, black phosphorus, and boron nitride. The mechanism of catalysts is complicated because the conversion reaction of sulfur with Li metal usually consists of four different stages: solid–liquid process, liquid–liquid process, liquid–solid process, and solid–solid process (Figure 1.7) [76]. Moreover, different polysulfides show different solubilities and physical properties in different electrolytes. Therefore, comprehensive understanding of how catalysts work is essential to guide the further designing of

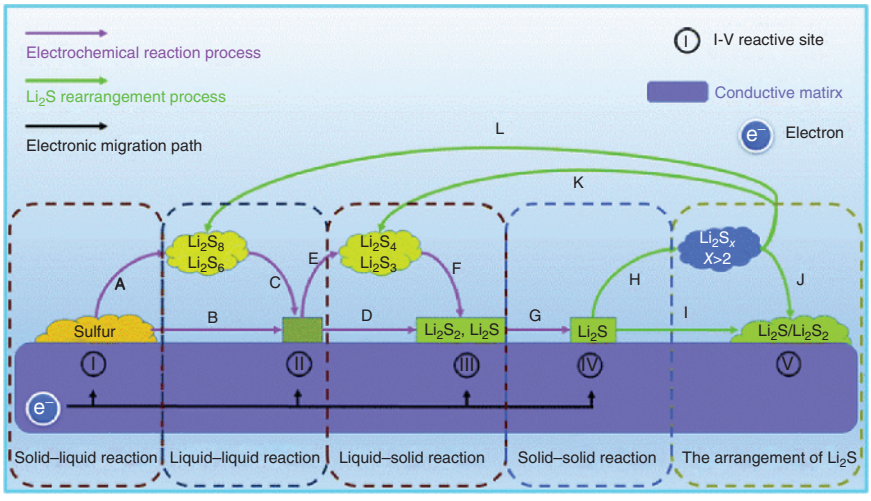

Figure 1.7 The electrochemical reaction process of the sulfur electrode. Source: Reproduced with permission Deng et al. [76].

suitable catalysts to achieved fast conversion kinetics and long-life Li–S batteries. The binding energy of different catalysts with Li_2S_6 was calculated by Y. Cui's group [88], indicating higher binding energy can lead to a better anchoring effect, thereby to mitigate polysulfide dissolution and suppress the shuttle effect. However, higher binding energies do not guarantee faster conversion kinetics because if the binding energy is too high to prevent the contact between polysulfides with conductive matrixes, it will lead to lower specific capacity and fast capacity decay.

1.2.2.2 Modifying Separators of Li–S Batteries

Separator is also one of the most components in Li–S batteries, which can directly prevent direct contact with cathode and anode, but allow the transportation of ions. Commercial separators used in Li–S batteries are polyolefin porous membranes, such as polyethylene (PE), polypropylene (PP), or multilayer composite membranes (PEP), which all have a pore size of about 100 nm. Big pores allow soluble polysulfides to pass through, leading to the shuttle effect. The modified separators can keep the dissolved polysulfides into the cathode side via the physical or chemical adsorption mechanism to improve the utilization of active materials and enhance the long-term cycling stability [89]. Manthiram's group first reported a microporous carbon film as an interlayer between the cathode and separator to block soluble polysulfides into the cathode area and suppress the shuttle effect (Figure 1.8a) [90]. In addition, the interlayer can be regarded as a current collector to improve the utilization of active materials. Later, they directly coated ultralight multiwall carbon nanotube (MWCNT) layers on the commercial PP separator. The MWCNT layers could effectively trap polysulfides and improve the cycling stability.

Similarly to the cathode matrixes, separators decorated by materials having strong chemical bonds with polysulfides were also reported. Separators coated with lightweight B- and N-doped reduced graphene oxides (rGO) were also prepared

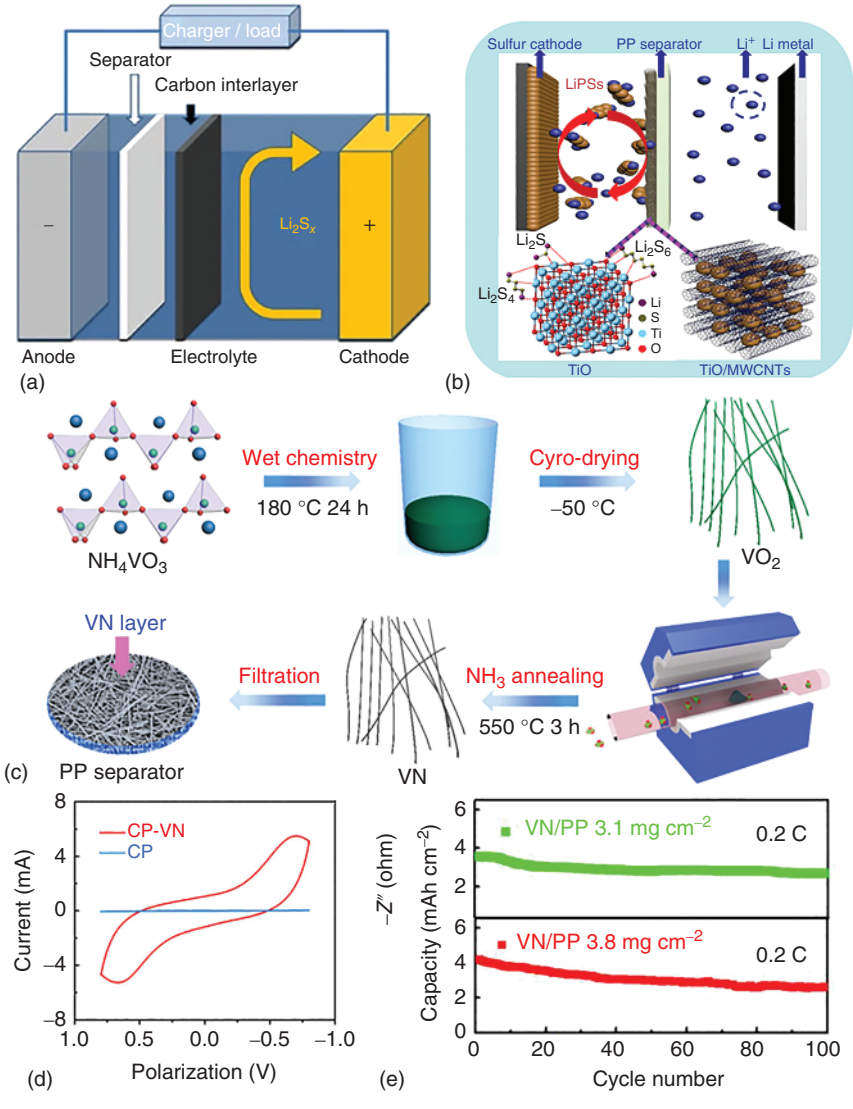

Figure 1.8 (a) Schematic configuration of a Li–S cell with a bifunctional microporous carbon interlayer. Source: Reproduced with permission Su et al. [90]. (b) Schematic configuration of TiO/MWCNTs coated separator for suppressing the shuttle effect. Source: Reproduced with permission Li et al. [91]. (c) Schematic showing the fabrication process of the VN-modified separator; (d) CV of symmetric cells using CP–VN and CP as electrodes; (e) cycling stabilities of S@VN/PP with sulfur mass loadings of 3.1 and 3.8 mg cm^{-2} at 0.2 C. Source: Song et al. [92] / with permission of American Chemical Society.

as a polysulfide reservoir [93]. The heteroatoms on rGO could create polar carbon lattices to form strong interaction with polysulfides, thus suppressing the shuttle effect. The commercial titanium monoxide (TiO) and MWCNTs coated separator was designed by Wang and coworkers (Figure 1.8b), which is a simple and low-cost process [91]. Compared with TiO_2, TiO offers higher conductivity, and based on the DFT calculation results, TiO has better adsorption effect. The Li–S batteries based on TiO/MWCNTs coated separator delivered a high capacity of 1033.8 mAh g^{-1} at 0.5 C with an ultralow fading rate of 0.057% per cycle. Metal-based materials were also used to decorate separators, due to their strong interaction with polysulfides as well as the catalytic effect they offered. VN-membrane-based separator was prepared by Sun and coworkers (Figure 1.8c) [92]. Due to excellent electronic conductivity of VN ($\sim 1 \times 10^6$ S m^{-1}), the VN-coated separator not only can act as a chemical reservoir to trap polysulfides but also can promote the redox kinetics (Figure 1.8d). Thus, Li–S batteries with VN-based separator delivered a low decay rate about 0.077% per cycle at 1 C for 800 cycles. A high areal capacity of 4.2 mAh cm^{-2} at 0.2 C can be obtained even with a high mass loading of 3.8 mg cm^{-2} (Figure 1.8e), indicating high sulfur utilization because of effective polysulfides trapping and fast redox kinetics induced by VN.

Modified separators can indeed suppress the shuttle effect and improve the cycling stability. However, multifunctional modified separators should be paid more attention. For example, materials used to modify separators could not only chemically adsorb polysulfides, but also can promote the conversion kinetics of polysulfides. In addition, modified separators will not affect the transportation of ions or increase the interface resistance. All these factors should be considered when designing suitable materials to decorate separators.

1.2.2.3 Electrolyte Design for Li–S Batteries

The electrolyte is one of important parts in batteries, which should have good ionic conductivity. In Li–S batteries, electrolyte is more important because the discharge intermediates are soluble in ether-based electrolytes (1,3-dioxolane [DOL]/DME based electrolytes), which are currently the best electrolyte systems in Li–S batteries with high ionic conductivity and suitable polysulfides dissolution. The challenges are to inhibit the shuttle effect and minimize the effect of polysulfides on Li metal anodes. Controlling the solubility of solvents is the most direct and effective method, such as choosing suitable solvents or adding cosolvents to optimize the solubility of polysulfides [94]. Among all kinds of solvents, fluorinated ethers solvents are widely applied in Li–S batteries as cosolvents because they can improve the viscosity of electrolytes and improve the mass-transfer process [95]. In addition, chelating oxygen by fluorine could change the solvation properties of fluorinated ethers, which can affect the solubility of lithium salts or polysulfides in electrolytes. Fluorinated diether (FDE) was reported by Wen's group as a cosolvent in the electrolyte of 1 M LiTFSI in DOL/DME [95]. Due to the insolubility of polysulfides in FDE, dissolution of polysulfides in the FDE modified electrolyte was suppressed. In addition, the corrosion of the Li metal anode was also decreased. As a result, the Li–S batteries with this optimized electrolyte exhibited a high reversible capacity of

701 mAh g^{-1} at 0.5 C after 200 cycles with an average coulombic efficiency of 99% (Figure 1.9a–c).

Another promising strategy is to increase the Li salt concentration. Because in the concentrated electrolytes, the solvents will form contact ion pairs (CIPs) or aggregates (AGGs) and the free solvents will disappear, resulting in insolubility of polysulfides [98–100]. Many researchers have reported that when the concentration of electrolytes is up to 5 M, both dissolution and diffusion of polysulfides decrease, leading to high coulombic efficiency of over 99%. However, with the increasing concentration, the ionic conductivity decreases, and voltage polarization is more obvious. Solid-state electrolytes (SSEs) were also explored in Li–S batteries. In SSEs, S can be directly transferred to Li_2S without producing soluble polysulfides; thus the shuttle effect and dissolution of polysulfides are both eliminated. Although the cycling stability of Li–S batteries can be improved, poor rate capability and high interfacial resistance are observed at room temperature due to low ionic conductivity. To date, numerous SSEs have been reported by researchers [101–103], including mainly inorganic solid electrolytes, solid polymer electrolytes, and composite solid electrolytes. In 2017, Tu's group reported an MoS_2-doped Li_2S-P_2S_5 glass–ceramic electrolyte ($Li_7P_{2.9}S_{10.85}Mo_{0.01}$) [96], which shows a high ionic conductivity of 4.8 mS cm^{-1} at room temperature and a high specific capacity of 1020 mAh g^{-1} at 0.05 C was obtained in all solid Li–S batteries at room temperature (Figure 1.9d–g). $LiBH_4$ has also been used in SSEs due to its high ionic conductivity for Li ions (over 2 mS cm^{-1}). Unemoto and coworkers reported an all-solid-state Li–S battery based on $LiBH_4$ electrolyte at 120 °C [97]. Only one plateau appeared during the cycling process, indicating that dissolution of polysulfides is inhibited (Figure 1.9h). At 0.05 C, the Li–S batteries with $LiBH_4$ electrolyte delivered an initial discharge capacity of 1140 mAh g^{-1}, and after 45 cycles the capacity can be maintained at 730 mAh g^{-1} with coulombic efficiency nearly 100% (Figure 1.9i).

Although dissolution of polysulfides and shuttle effect were completely inhibited in SSEs, in terms of reaction kinetics and the demand for fast charging/discharging, the SSEs face many challenges, especially using high sulfur mass loading and less conductive matrixes. In order to explore optimized electrolytes for Li–S batteries, ionic conductivity, suitable solubility and diffusion of polysulfides, and stability with Li metal anodes all should be considered.

1.2.2.4 Anode Protection for Li–S Batteries

Lithium–sulfur batteries use Li metal as anode, because its chemical activity is high and Li metal can easily react with electrolyte, leading to low coulombic efficiency. In addition, the formation and growth of Li dendrites on anode surface will hinder practical applications of Li–S batteries. Due to the shuttle effect, polysulfides will also react with Li metal and corrode the Li metal anode. The protection strategies for Li metal anodes in Li–S batteries include: exploring electrolyte additives to form stable SEI layer, forming artificial SEI by coating materials on the surface of Li metal and using alloy anode [104–106].

Among the electrolyte additives, $LiNO_3$ is widely used in Li–S batteries, which expertly can improve the cycling stability of Li–S batteries. Xiong's group explained

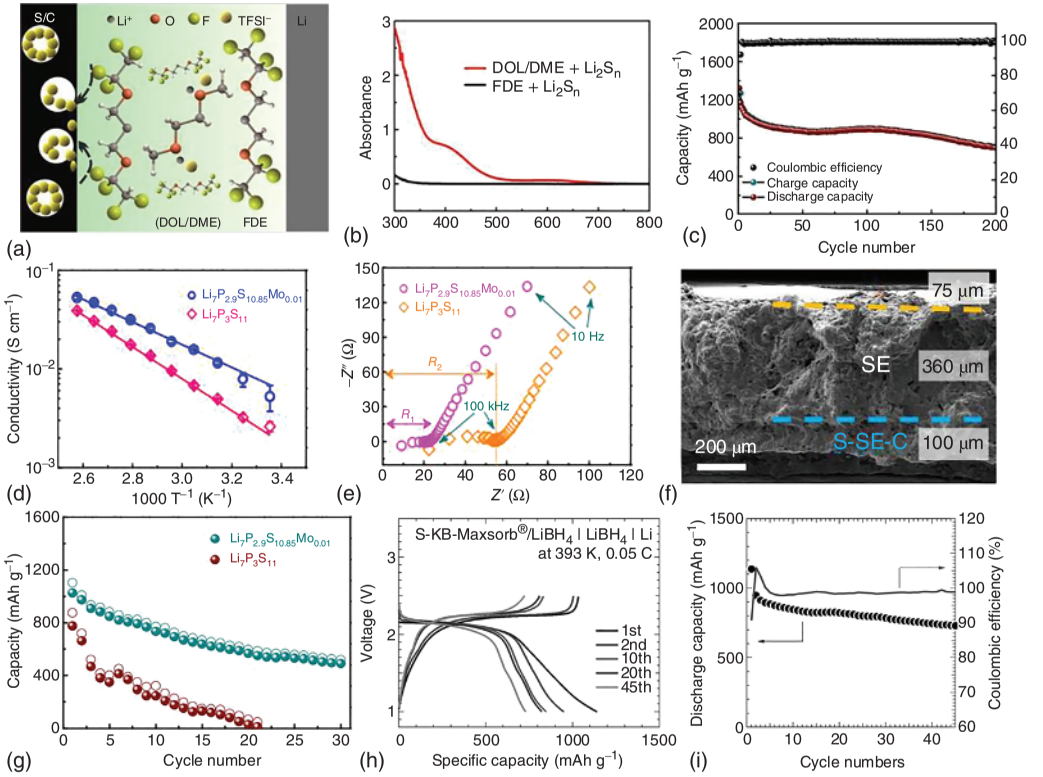

Figure 1.9 (a) Schematic diagram of fluorinated diether cosolvent electrolytes in Li–S batteries. (b) Ultraviolet–visible (UV–vis) spectra of polysulfides in different solvents; (c) cycle performance of Li–S batteries with 80% FDE electrolyte at 0.5 C. Source: Reproduced with permission Gu et al. [95]. (d) Arrhenius conductivity plots of $Li_7P_3S_{11}$ and $Li_7P_{2.9}S_{10.85}Mo_{0.01}$ at temperatures from 298 to 388 K. (e) Impedance plots of the electrolytes at room temperature; (f) cross-sectional SEM images of all-solid-state Li–S battery based on $Li_7P_{2.9}S_{10.85}Mo_{0.01}$ electrolyte; (g) cycling performances of $Li_7P_3S_{11}$ and $Li_7P_{2.9}S_{10.85}Mo_{0.01}$ as the electrolytes for all-solid-state Li–S batteries at a rate of C/20 at room temperature. Source: Xu et al. [96] / with permission of Royal Society of Chemistry. (h) Typical discharge–charge profiles of the S-KB-Maxsorb/$LiBH_4$|$LiBH_4$|Li rechargeable cell operating at 393 K and 0.05 C. (i) Discharge capacity and coulombic efficiency as a function of cycle numbers. Source: Reproduced with permission Unemoto et al. [97].

that $LiNO_3$ can react with Li metal to form a stable SEI layer [107], consisting of both inorganic species of LiN_xO_y and organic species such as ROLi and $ROCO_2Li$, which can effectively suppress the shuttle effect to protect Li metal anodes. Zhang and coworkers investigated the role of the SEI layer by *operando* the X-ray absorption spectroscopy (XAS) technique [108], indicating a dense and stable SEI layer composed of Li_2SO_3 and Li_2SO_4 formed in the first discharge process due to the synergistic effect of shuttled polysulfides and $LiNO_3$, which can effectively suppress the shuttle effect and protect Li metal anodes (Figure 1.10a). The P_2S_5 was also reported as electrolyte additive in Li–S batteries [111], which can react with Li_2S to generate soluble composites to promote the conversion of Li_2S. In addition, the SEI formed on Li metal can prevent the direct contact between the electrolyte with soluble polysulfides to suppress the corrosion of Li metal. The cycling stability of Li–S batteries was dramatically increased after the addition of P_2S_5 additive, delivering a specific capacity of 900 mAh g^{-1} after 40 cycles at 0.1 C.

Forming artificial SEI film by in situ or ex situ techniques has also been used to protect Li anode and inhibit lithium dendrites [112–114]. An ideal artificial SEI should have the following advantages: good chemical stability, excellent ionic conductivity for Li ion diffusion, and good mechanical strength to accommodate the Li dendrites. A poly(vinylidene fluoride)-*co*-hexafluoropropylene (PVDF-HFP) and lithium fluoride (LiF) formed freestanding layer was prepared to protect Li metal anodes [115], offering a synergistic soft-rigid feature. This kind of protective layer can realize dendrite-free Li metal anodes, as well as can greatly reduce interfacial resistance due to suppression of random Li deposition and formation of isolated Li. Choi and coworkers developed a 10-nm-thick two-dimensional (2D) MoS_2 layer as a protective layer on Li metal through sputtering deposition (Figure 1.10b) [109]. The Li atoms can insert into the layered MoS_2 structure, resulting in low interfacial resistance and fast Li ion flow rate. In addition, high conductivity of the MoS_2 interlayer could lead to the uniform deposition of Li ions and eliminate the growth of Li dendrite nucleation.

Replacing Li metal with micro/nanostructured hybrid composites is another promising method to guide the Li deposition and accommodate the volume changes during striping/plating process. The nanosized Li metal host with rich porosity, high surface area, and connected conductive channels can lead to unique deposition behavior of Li ions and improve the safety of Li metal anodes. Cui and coworkers designed a polymeric matrix with the lithiophilic property to load molten Li metal [110], resulting in a nanofiber porous Li anode (Figure 1.10c). In addition, the polymeric matrix can trap Li into its backbones to accommodate the volume change and suppress the growth of Li dendrites (Figure 1.10d). The high surface area of porous Li metal anodes can reduce the effective current density. Owing to the above advantages, the batteries can deliver a stable cycling performance of more than 100 cycles even at a high current density of 5 mA cm^{-2} in both carbonate and ether electrolytes. Li-alloying materials have received much attention due to their good processability and excellent theoretical capacity (3495 mAh g^{-1}). It has been reported Li–B alloy indeed could change the behavior of Li deposition. For example, Zhang and coworkers used Li–B alloy as anode instead of Li metal [116]. The alloy

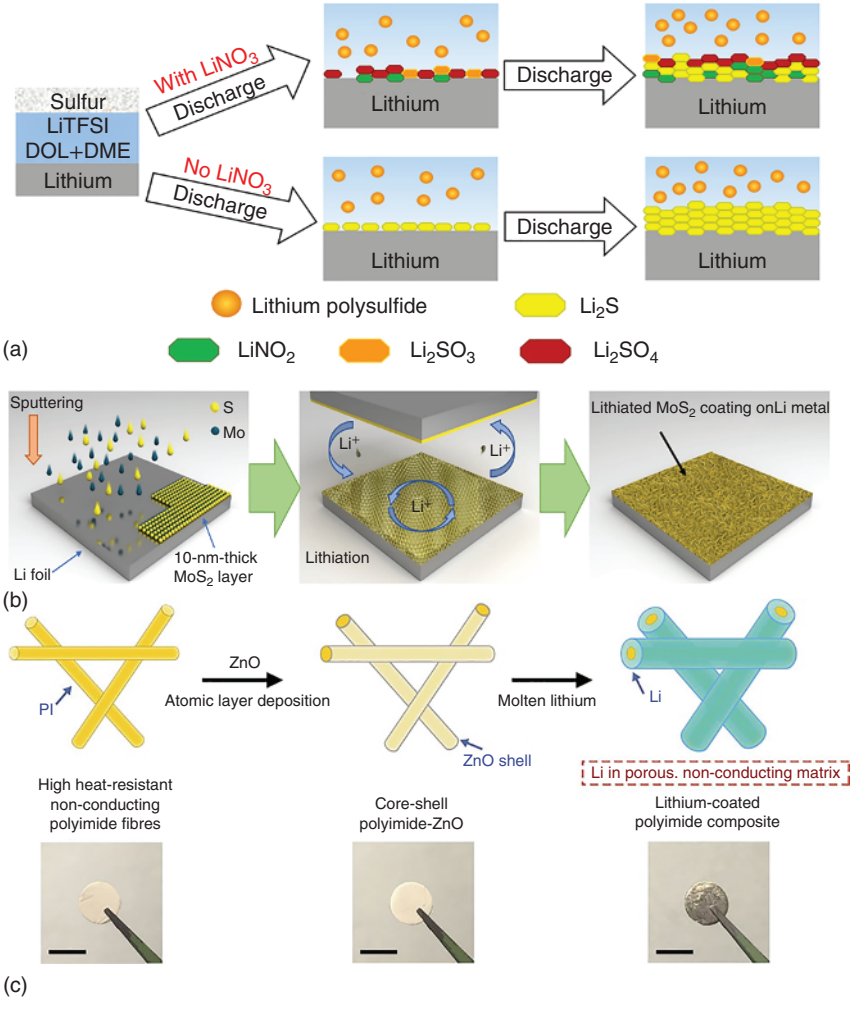

Figure 1.10 (a) Illustration of $LiNO_3$ additives for suppressing the shuttle effect. Source: Reproduced with permission Zhang et al. [108]. (b) Schematics illustrating the fabrication method for a MoS_2-coated Li anode via sputtering and subsequent lithiation. Source: Reproduced with permission Cha et al. [109]. (c) Electrospun PI was coated with a layer of ZnO via ALD to form core–shell PI-ZnO. The existence of ZnO coating renders the matrix "lithiophilic" such that molten Li can steadily infuse into the matrix. The final structure of the electrode is Li coated on a porous, nonconducting polymeric matrix. Source: Liu et al. [110] / with permission of Macmillan Publishers.

has unique structure with abundant free Li embedded in stable Li_7B_6 loofah sponge-like framework. The Li_7B_6 component could suppress the orientational deposition of Li ions, reduce effective current density, and promote the formation of stable SEI layers, resulting in stable Li–S batteries.

Until now, huge attention has been paid to Li–S batteries, including exploring conductive matrixes for sulfur, modifying separators to suppress the shuttle effect,

exploring suitable electrolytes, and designing strategies to protect Li metal anodes. Great achievements have been made to increase the long-term cycling stability. But in view of practical applications, lean electrolytes and high mass loading should be considered, which are generally are paid less attention. The preparation process of sulfur host needs to be as simple as possible. To further understand anode and electrolyte degradation as well as the components and structures of electrolyte interfaces, new analytical tools and in situ techniques should be applied. If these problems are solved, Li–S batteries will take great strides toward their practical applications.

1.2.3 Lithium–Selenium or –Tellurium Batteries

As members of chalcogens (group VIA elements), like sulfur, selenium (Se) and tellurium (Te) have also been studied as cathode materials for Li metal batteries [10, 117–119]. Although gravimetric capacity of Se (675 mAh g^{-1}) and Te (419 mAh g^{-1}) is lower than that of S cathode (1675 mAh g^{-1}), gravimetric capacity of Se (3246 mAh cm^{-3}) and Te (2621 mAh cm^{-3}) is comparable with that of S cathode (3416 mAh cm^{-3}). In addition, Se (1×10^{-3} S m^{-1}) and Te (2×10^{2} S m^{-1}) exhibit better electronic conductivity compared to S (5×10^{-28} S m^{-1}), with additional advantages such as better rate capability and high utilization of active materials. Basic physicochemical properties and related practical performance of S, Se, and Te are compared in Figure 1.11a,b [120].

Although Li–Se/Te batteries exhibit some advantages, practical applications are still hindered by their intrinsic properties, such as soluble intermediates, positive electrode volume expansion, and the growth of lithium dendrites. Therefore, great efforts have been made to improve the cycling stability of Li–Se/Te batteries. In this section, we mainly discuss the reaction mechanism, optimization of cathode structures, and Li metal anode protection.

1.2.3.1 Lithium–Selenium Batteries

1.2.3.1.1 Mechanism of Li–Se Batteries

Amine and coworkers initially reported Se/MWCNTs composites as cathode for Li–Se batteries in a carbonate electrolyte [121]. There is only one redox plateaus pair during discharge/charge process, indicating the direct conversion between Se and Li_2Se without any polyselenides (Figure 1.11c). This result is different from that of S cathode in ether-based electrolytes, which is a multiple reaction mechanism. Some researchers believed that insolubility of polyselenides in carbonate electrolytes is responsible for single-phase transformation [122]. However, some relevant works showed that multistep lithiation in carbonate electrolytes makes the working principle still ambiguous. For example, Zhou's group reported that Se nanowire cathodes exhibited multi-plateaus during cycling process in carbonate electrolytes [123]. After a large number of studies, it has been reported that the crystal structure of Se has a critical impact on the lithiation process, where amorphous Se appears in multistep lithiation, while trigonal Se delivers single-phase transformation [124, 125]. Similar to S, lithiation/delithiation of Se in ether-based electrolytes

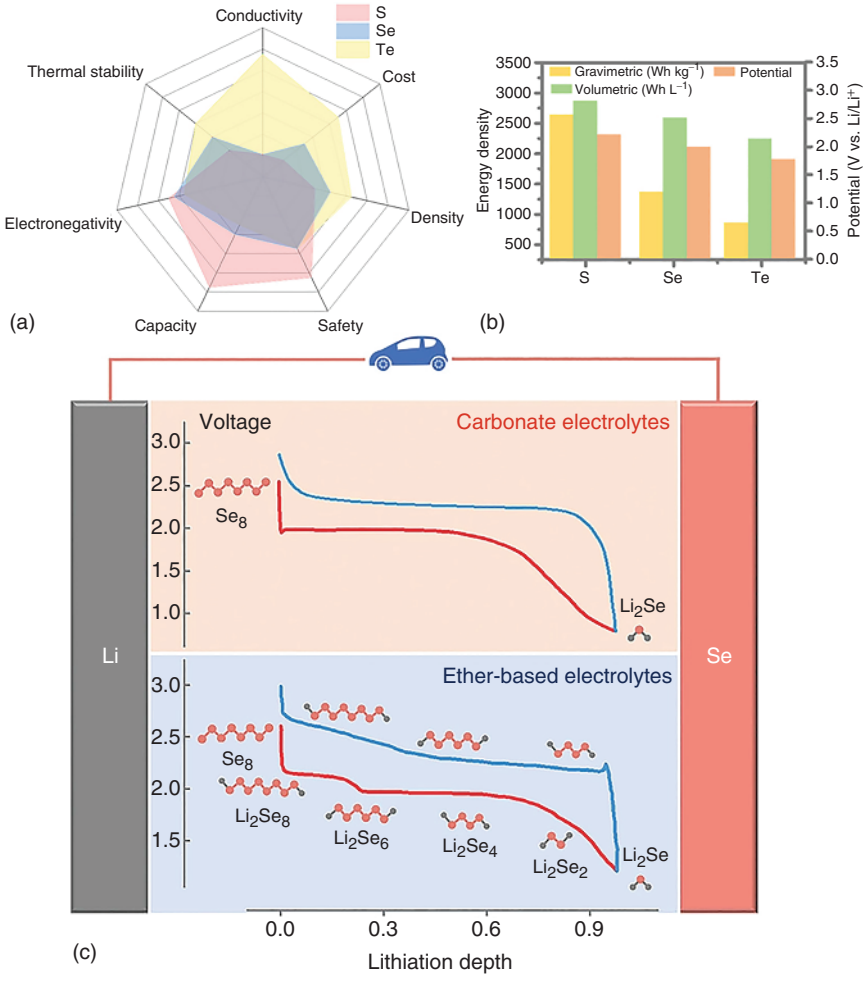

Figure 1.11 (a) Comparison of S, Se, and Te based on various properties. (b) Energy density and plateau voltage of Li–S, Li–Se, and Li–Te batteries. Source: Reproduced with permission Chen et al. [120]. (c) Schematic of the charge/discharge behaviors of Li–Se batteries in carbonate and ether-based electrolytes. Source: Reproduced with permission Sun et al. [10].

shows multiple conversion processes with a lower redox potential (Figure 1.11c) [126]. Generally, Se is first reduced to Li_2Se_n ($n \geq 4$) at ≈2.1 V, then to Li_2Se_2, and finally to Li_2Se at ≈1.9 V. While in the charge process, Li_2Se is directly oxidized to Li_2Se_n ($n \geq 4$) at ≈2.3 V by passing Li_2Se_2, and eventually to Se [127]. Polyselenides are soluble in ether-based electrolytes, which could lead to the "shuttle effect" similarly to sulfur cathode. Although the shuttle effect is not present in carbonate electrolytes, strong nucleophilic reactions between chain-like Se anions and the carbonyl groups of organic solvent will lead to severe capacity fading. Therefore, the major challenge of Li–Se batteries is to inhibit the shuttle effect and improve

the cycling stability of Se cathode. Great efforts have been made to improve the electrochemical performance of Li–Se batteries [128–130], including designing suitable nanostructured Se cathodes, modifying separators to suppress the shuttle effect, and exploring SSE. In the following section, we discuss these strategies in detail.

1.2.3.1.2 Cathode Design for Li–Se Batteries

Due to its good electronic conductivity, Se can be directly used as a cathode material. Different kinds of nanostructured Se materials have been prepared, such as nanowires [123], thin films [131], and 3D frameworks [132]. But due to the inevitable side reaction and the shuttle effect, the cycling stability of pure Se nanomaterials is inferior. Thus, a host material is needed to overcome these problems. Ideal host materials should have the following properties: (i) high volume ratio to load Se; (ii) special channels or walls to protect Se from side reactions; (iii) good conductivity and good mechanical properties to accommodate volume changes. In this part, carbonaceous materials are first summarized as Se host. Then, heteroatom-doped carbon or metal-based-material-modified carbon are designed to chemically trap polyselenides. Se embedded into organic composites and Se alloys are also discussed.

To inhibit the shuttle effect, surface coating is a simple and effective method. Eom and coworkers presented conductive PANi layer coated Se/C (ET-Se/C/aniline) composites through electrochemical polymerization as the cathode material for Li–Se batteries (Figure 1.12a) [133]. The C—N bonds in the PANi layer could trap soluble Li_2Se_n to improve the cycling stability. As a result, the designed PANi coated Se/C exhibited high initial capacities of 596 mAh g^{-1} and 2873 mAh cm^{-3}, which can be maintained to 462 mAh g^{-1} and 2227 mAh cm^{-3} after 200 cycles with a retention rate of 78%. A microporous carbon (MPC) matrix consisting of a MWCNT core coated by a microporous carbon sheath was prepared to host Se (Figure 1.12b) [134]. Electrochemistry of a Li–Se_x battery was investigated by Raman spectra and theoretical calculations, indicating that the Se_x confined into the micropores undergoes a single-step reaction from Se_x directly to Li_2Se (Figure 1.12c).

The flexible and freestanding matrixes were also investigated as host materials for Se [137, 138]. Yu's group designed a porous carbon nanofibers (PCNFs)/selenium composite electrode (Se@PCNFs) by infiltrating Se into mesoporous carbon nanofibers (PCNFs) (Figure 1.12d,e) [135]. The mesopores can load high mass Se and simultaneously suppress the dissolution of active materials. When paired with Li metal, the Se@PCNFs electrode exhibits a reversible capacity of 516 mAh g^{-1} after 900 cycles without any capacity loss at 0.5 A g^{-1}. A 3D graphene-CNT@Se (3DG-CNT@Se) aerogel with carbon nanotube/selenium sandwiched between graphene nanosheets is reported by He and coworkers (Figure 1.12f) [136]. The unique 3D mesoporous, conductive network provides effective channels for electron transfer and ionic diffusion, and the hierarchical structure could suppress the dissolution of polyselenides and accommodate the volume expansion of Se during cycling. As a result, the 3DG-CNT@Se delivered an initial capacity of 632.7 mAh g^{-1} and good rate capability (high capacity of 192.9 mAh g^{-1} at 4 C).

To further improve the cycling stability of Se/C composites, carbon-based matrixes with chemical adsorption sites for polyselenides were also studied [139–141].

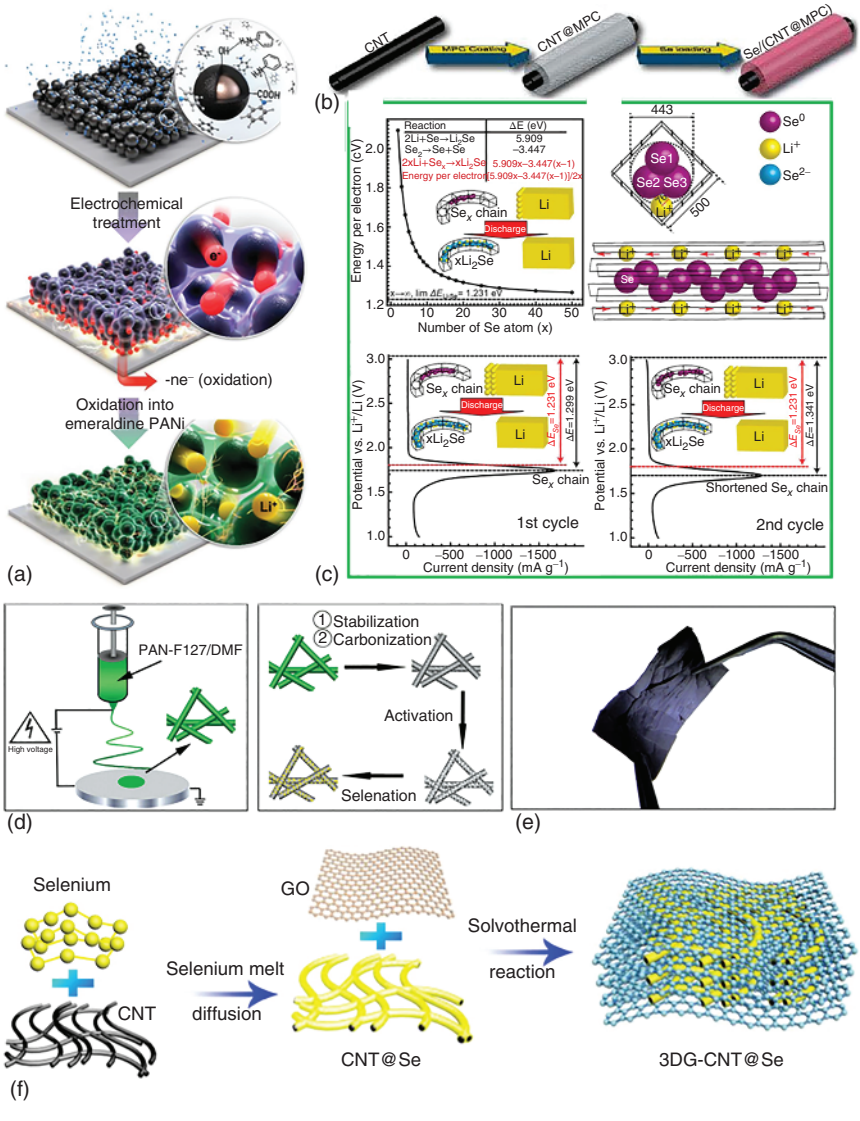

Figure 1.12 (a) Schematic illustration of the electrochemical polymerization of aniline on a Se/C cathode. Source: Reproduced with permission Lee et al. [133]. (b) Schematic diagram showing the preparation of Se/(CNT@MPC); (c) electrochemistry of a Li–Se_x battery. Source: Reproduced with permission Xin et al. [134]. (d) Schematic illustration of the synthesis process and (e) photograph of the Se@PCNFs electrode. Source: Zeng et al. [135]. Reproduced with permission of (2014) John Wiley and Sons. (f) Schematic illustration of the synthesis procedure of the 3DG-CNT@Se composite. Source: Reproduced with permission He et al. [136].

In 2017, metal–organic framework (MOF) derived cobalt and nitrogen-doped porous graphitic carbon (C–Co–N) was prepared by He's group (Figure 1.13a) [142]. Owing to the unique structure with abundant micro-/mesopores, the highly conductive C–Co–N matrix provides highly efficient channels for electron transfer and ionic diffusion. Uniform distribution of Co nanoparticles and nitrogen groups in the composite can anchor polyselenides through strong chemical interaction (Figure 1.13b). With a very high Se loading of 76.5 wt%, the C–Co–N/Se cathode delivers superior electrochemical performance with an ultrahigh initial reversible capacity of 672.3 mAh g^{-1} and a capacity of 574.2 mAh g^{-1} after 200 cycles. Single cobalt atoms were also introduced to N-doped hollow porous carbon by Wang's group (Figure 1.13c) [143]. Cobalt single atoms can activate selenium reactivity and immobilize selenium and polyselenides. The as-prepared selenium–carbon (Se@CoSA-HC) cathodes deliver an ultra-long cycling stability over 5000 cycles at a high current density of 50 C almost with no capacity fading (Figure 1.13d).

Selenium sulfides were also selected as cathode materials because Se and S have many common grounds for Li batteries. In addition, introducing S into Se can increase the capacity of Se cathode [121, 127, 144]. Lou's group developed a free-standing, lotus root-like carbon fiber network decorated with CoS_2 nanoparticles (denoted as CoS_2@LRC) as the SeS_2 host for enhancing the lithium storage performance (Figure 1.14a) [145]. The CoS_2 nanoparticles were uniformly distributed on the inner walls of carbon fibers, providing efficient sulfiphilic sites for restricting the dissolution of polysulfides and polyselenides during cycling processes. In addition, the 3D interconnected multichannel carbon fibers provide excellent electron and ion transport (Figure 1.14b). Thus, the CoS_2@LRC/SeS_2 materials delivered a high

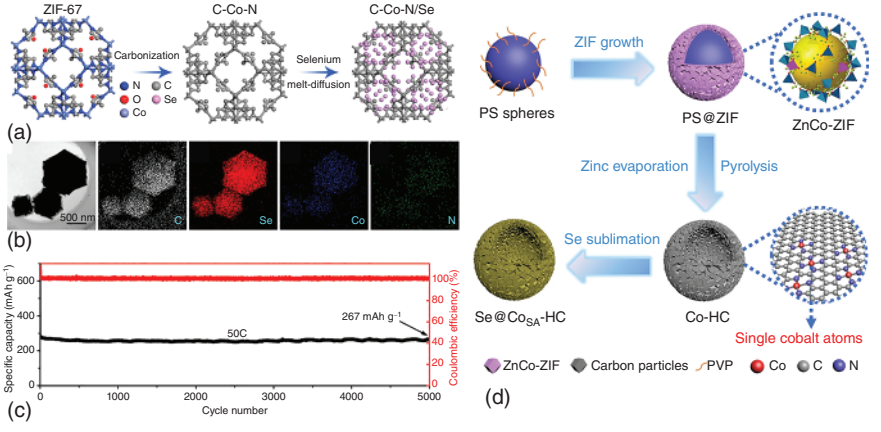

Figure 1.13 (a) Schematic illustration of the synthetic process for C–Co–N/Se; (b) the TEM image of C–Co–N/Se and the corresponding elemental mapping images of carbon, selenium, cobalt, and nitrogen. Source: He et al. [142] / with permission of Elsevier. (c) Schematic illustration of synthesizing procedures for cobalt single atoms/nitrogen-doped hollow porous carbon (CoSA-HC) particles; (d) long cycling performance and coulombic efficiency of Se@CoSA-HC at 50 C for 5000 cycles. Source: Tian et al. [143]. Licensed under CC BY 4.0.

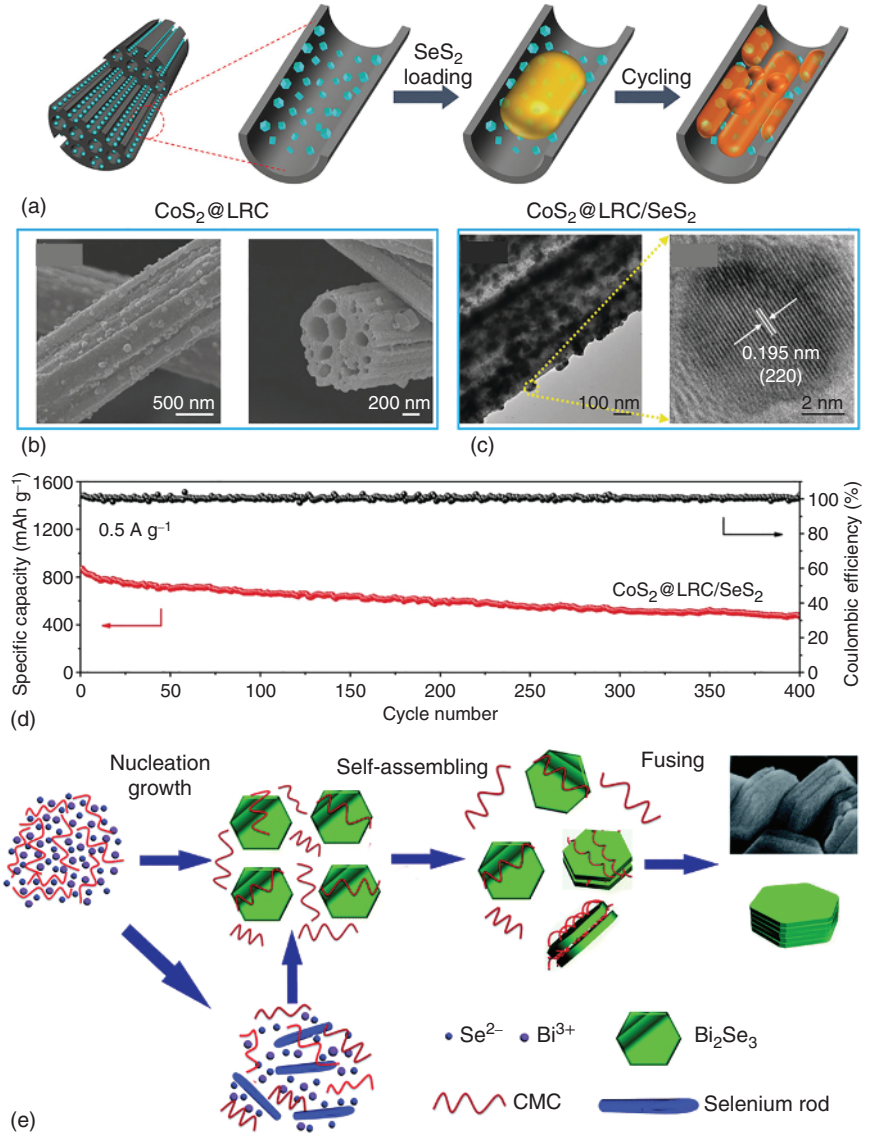

Figure 1.14 (a) Proposed advantages of CoS_2@LRC/SeS_2 on suppressing the dissolution of polysulfides and polyselenides. (b) SEM and TEM images of CoS_2@LRC; (c) prolonged cycle life of CoS_2@LRC/SeS_2 at 0.5 A g^{-1}. Source: Zhang et al. [145] / with permission of John Wiley and Sons. (d) Schematic illustration of the proposed formation mechanism of the Bi_2Se_3 stacking nanosheets. Source: Xu et al. [146]/ with permission of Royal Society of Chemistry.

capacity of 1010 mAh g^{-1} and a long cycling stability over 400 cycles at 0.5 A g^{-1} (Figure 1.14c). Bi_2Se_3 stacking nanosheets have been successfully synthesized by a "green" and facile approach (Figure 1.14d), which can exhibit an initial discharge capacity of 715 mAh g^{-1} due to their novel hierarchical architecture [146].

1.2.3.1.3 Electrolytes Modification and Anode Protection of Li–Se Batteries

The SSEs, in which polyselenides are insoluble, have been attracting much attention to solve the shuttle effect fundamentally [147–150]. However, low ionic conductivity is the main problem hindering their widespread application, as well as poor wettability between SSEs and active materials leads to increasing interface resistance [151, 152]. Exploration of SSEs for Li–Se batteries is still in its early stage; great effort should be devoted. A solid-state protective layer was applied on both Se cathode and Li metal anode by adding FEC additive into an ether-based electrolyte (Figure 1.15a) [153]. The solid protective layer can reduce the dissolution of Se cathode materials as well as guide uniform decomposition of Li_2Se (Figure 1.15b,c). To combine the merits of both liquid and SSEs, gradient solidification of conventional ether-based liquid electrolytes was designed by Guo's group, through a facile in situ interfacial polymerization (IsIP) process (Figure 1.15d,e) [154]. As a result, a polymer-based gel electrolyte formed on the surface of the cathode, while the liquid electrolyte was preserved inside the cathode. The hybrid electrolyte configuration enables moderate dissolution of discharge products inside the cathode while preventing the shuttle of soluble intermediates away from the cathode. As a result, Li–Se batteries deliver a

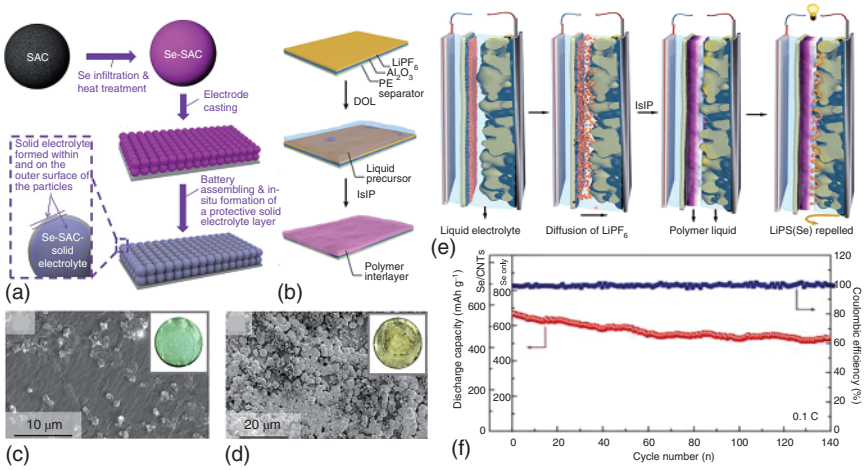

Figure 1.15 (a) Schematic illustration of formation of the protective layer on the Se cathode; SEM images of Li metal after one cycle with (b) FEC-enriched electrolyte and (c) a normal electrolyte. Source: Lee et al. [153] / with permission of Royal Society of Chemistry. (d) Schematic illustration showing in situ interfacial polymerization of a liquid electrolyte realized with the $LiPF_6/Al_2O_3$/PE separator. Source: Lee et al. [153] / with permission of Royal Society of Chemistry.; (e) schematic illustration showing the IsIP process of DOL induced by the $LiPF_6/Al_2O_3$/PE separator; (f) cycling performance and coulombic efficiency of Li–Se batteries with IsIP electrolyte at 0.1 C. Source: Reproduced with permission Wang et al. [154].

high initial specific capacity of 670 mAh g^{-1} and a high capacity retention of 83.5% after 140 cycles (Figure 1.15f).

Selenium has gained interest as cathode for Li–Se batteries due to its capacity density and high electronic conductivity. Numerous efforts have been made to designing nanostructured Se composite cathodes, exploring suitable electrolyte systems to suppress the shuttle effect, and improving the cycling stability. However, to promote the application of Li–Se batteries needs a lot of effort. For example, the mechanism of Se cathode in carbonate electrolytes is not clear. Some works indicate a single-conversion process, while others indicate a multiple-reaction process. In addition, due to the insolubility of polyselenides in carbonate electrolytes, in-depth researches need to be done with carbonate electrolytes instead of ether-based electrolytes. Finally, anode safety is also important in practical applications. More works on anode protection need to be designed, such as electrolyte additives, SSEs, or artificial SEI layer.

1.2.3.2 Lithium–Tellurium Batteries

Similar to Se, Te cathodes also receive relatively more attention [120, 155–158]. The huge problems are the "shuttle effect" of polytellurides and large volume expansion during cycling processes. To overcome these problems, the common strategies are to confine active materials into porous host materials to trap polytellurides and to accommodate the volume change [159].

He's group designed a rGO wrapped ultrathin tellurium nanowires (TeNWs) via a facile hydrothermal method as Te cathode for Li–Te batteries (Figure 1.16a) [160]. Due to the 3D framework and high conductivity of rGO, the 3DGT aerogel offers highly efficient channels for electron transfer and ionic diffusion, as well as good volume ratio for volume expansion (Figure 1.16b,c). Thus, the 3DGT shows a high initial capacity of 1685 mAh cm^{-3} at 1 C after 500 cycles (Figure 1.16d), showing remarkable long-cycle performance at high current density. Despite the nanostructured host materials, the cathode structure is also important to improve electrochemical performance. For example, some researchers confined Te into pores of host materials [164, 165], while others coated Te on the surface of host materials [166]. To compare these two different cathode structures, carbon nanotube aerogel was prepared by Yu and coworkers to host Te as cathode for lithium batteries [161]. Two different configurations of cathodes are designed: in configuration I, direct dropping Te solution on the surface of carbon nanotube aerogel; in configuration II, penetrating Te into the inner pores of carbon nanotubes (Figure 1.16e). When used as cathode materials for Li–Te batteries, configuration II exhibits much improved cycling performance due to the space confinement of nanopores to trap active Te molecules and the discharge product, while the elastic nature of the cathode helps to alleviate the deformation stress upon cycling.

Although the Te/carbon materials have exhibited excellent cycling stability, theoretical gravimetric capacity of Te is relatively low (420 mAh g^{-1}) [167, 168]. To address this problem, Te is combined with S element to form Te_xS_y composites, which can offer the merits of both elements, such as high conductivity of Te and high theoretical capacity of S [169]. Zhou's group confined heteroatomic Te_xS_{1-x}

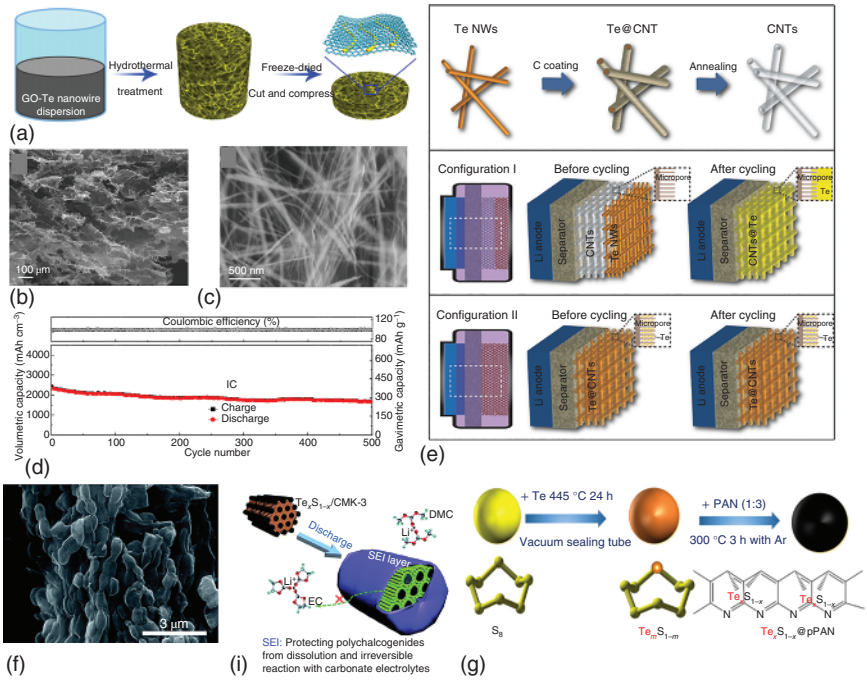

Figure 1.16 (a) Illustration of the formation process of the 3DGT aerogel and schematics of fabricating a self-supporting electrode; (b) low- and (c) high-magnification SEM images of 3DGT. Source: He et al. [160] / with permission of American Chemical Society. (d) Schematic illustration showing the typical synthesis procedures of the CNTs. (e) Configuration I using the TeNW/CNT cathode and its working principle. (f) Configuration II using the Te@CNT cathode and its working principle. Source: Xu et al. [161] / with permission of John Wiley and Sons. (g) SEM images of $Te_{0.1}S_{0.9}$/CMK-3; (h) schematic diagram of the Te-induced formation of SEI layers on the Te_xS_{1-x}/CMK-3 electrode surfaces. Source: Reproduced with permission Sun et al. [162]. (i) Synthetic schematic and the morphology characterization of $Te_{0.04}S_{0.96}$@pPAN. Source: Reproduced with permission Li et al. [163].

molecules into ordered mesoporous carbon CMK-3 via a facile melt-impregnation route (Figure 1.16g) [162]. The Te—S bonds in the heteroatomic Te_xS_{1-x} molecules offer higher intrinsic electrical conductivity and electrochemical reaction activity than the homoatomic S_8 molecules. Moreover, Te-containing polychalcogenide intermediates could help to form an SEI layer on Te_xS_{1-x}/CMK-3 surfaces, which can prevent polychalcogenides from the shuttle effect and side reactions with the carbonate solvent (Figure 1.16h). In addition, the mesopores on CMK-3 could confine the polychalcogenide intermediates. As a result, the $Te_{0.1}S_{0.9}$/CMK-3 composites can maintain a high reversible capacity of 845 mAh g^{-1} after 100 cycles at 250 mA g^{-1}.

To improve the slow kinetics of sulfurized polymer cathode [170, 171], Xie and coworkers used Te as an eutectic accelerator in S@pPAN to accelerate the redox conversion and prevent polysulfides dissolution (Figure 1.16i) [163]. In the Te-doped S@pPAN cathodes, Te can be uniformly distributed through Te—S bonds.

In addition, Te could contribute to improve capacity during the cycling process. Thus, Te-doped S@pPAN cathodes delivered high capacities and stable cycling over 600 cycles in the ether electrolyte (0.05% decay per cycle).

Until now, Te cathodes have received less attention than S cathodes due to their low theoretical gravimetric capacity. Heteroatomic Te_xS_{1-x} composites may be a promising candidate to improve gravimetric capacity. Although great achievements have been made on Te cathodes, the cycling stability is still far away from practical applications. Therefore, more efficient host materials and optimized systems need to be largely explored.

1.2.4 Lithium–Iodine/Bromine Batteries

With the emergence of hybrid grids and electric vehicles, there is an urgent need to develop energy storage devices with high energy density and power density. Nowadays, Li metal batteries paired with conversion type cathodes, such as S and O_2, have drawn much attention. But undeveloped discharge capacity and poor electrochemical reversibility of S and O_2 cathodes make them hard for practical applications. The shuttle effect of intermediates in Li–S batteries and the slow kinetic reactions of O_2 cathode need to be addressed before their commercialization. Therefore, exploring advanced novel batteries with redox reaction is urgently needed. Halogens (I_2 and Br_2, but not F_2 and Cl_2, which are gases and toxic) can be used in energy storage systems [172]. Bromine and iodine can provide relatively high specific capacities of 310 and 211 mAh g^{-1}, respectively. Moreover, the redox pairs of Br^{3-}/Br^- and I^{3-}/I^- have good reversibility with redox potentials at 1.07 and 0.54 V vs. SHE (standard hydrogen electrode). Although the specific capacity is low, but high voltage output can lead to high energy density. In addition, I_2 and Br_2 with good chemical/physical stability and low cost seem to be the promising alternative cathodes. In this section, we summarize the mechanism of Li–I_2/Br_2 batteries, then discuss the strategies made to improve electrochemical performance, and finally provide some suggestions.

1.2.4.1 Lithium–Iodine Batteries

1.2.4.1.1 Mechanism of Li–I_2 Batteries

Actually, as an abundant source in oceans, iodine has a long and profound history as a cathode material applied in batteries [173, 174]. The fundamental redox reactions involving iodine-based batteries can be described as follows (Figure 1.17) [175]:

On discharge process:

$$3I_2 + 2e^- = 2I_3^-$$

$$I_3^- + 2e^- = 3I^-$$

On charge process:

$$3I^- - 2e^- = I_3^-$$

$$2I_3^- - 2e^- = 3I_2$$

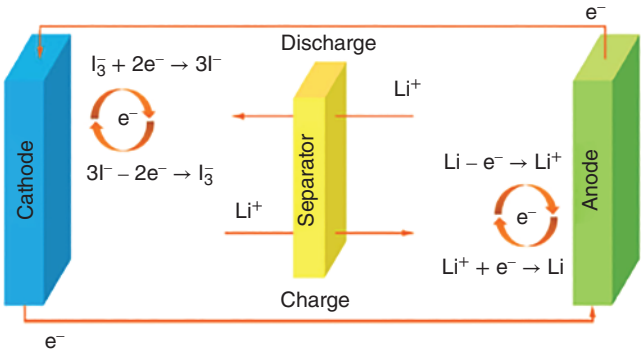

Figure 1.17 The working concept of the I_3^-/I^- redox reaction in an aqueous Li-I_2 battery. Source: Reproduced with permission Ma et al. [175].

The formation of soluble I_3^- ions and the dissolution of I_2 in the electrolyte decrease the utilization of active materials and lead to the shuttle effect, which can cause the corrosion of Li metal anodes, resulting in low columbic efficiency, poor cycling performance, and short lifetime of Li–I_2 batteries, which are the bottlenecks of Li–I_2 batteries [13, 173, 176].

1.2.4.1.2 Cathode and Interlayer Modification of Li–I_2 Batteries

To solve the aforementioned problems, numerous researches have been done. Similar to S cathodes, carbonaceous materials are widely used as matrixes to host I_2 [177–179]. In 2017, Liu's group applied active graphene (AG) to load high mass of I_2 (56 wt%), through an in situ deposition method (Figure 1.18a) [180]. The AG has a large specific surface area, abundant micropores and mesopores, free interparticle voids, and unimpeded ion diffusion channels. The as-prepared high mass loading I_2-AG composite delivers high capacity (218 mAh g^{-1} at a 1 C), stable cycling stability (capacity fading rate of only 0.023% per cycle), and good rate capability (184 mAh g^{-1} at a 20 C). These results indicate the nanopores in AG could effectively protect the I_2 from dissolution and improve the cycling stability. Recently, they further coated the I_2/AG with several kinds of polymers, such as methyl-beta-cyclodextrin (MβCD), polyvinylpyrrolidone (PVP), and amylose corn starch (ACS) [182]. The polymer can chemically react with I_2 to form inclusion complexes on the surface of I_2/AG composites. The formed inclusion complexes can effectively inhibit the dissolution of iodine into the electrolyte. As a result, the polymer-modified I_2/AG composites show enhanced electrochemical performance in terms of cycling stability and coulombic efficiency. Adding a block interlayer between cathode and separator is a direct way to suppress the shuttle effect [183]. Zhang's group synthesized honeycomb-like carbon materials (HCMs) via a "salty" thermal treatment of coffee extract to be applied as an interlayer to block the dissolution of I_2 (Figure 1.18b) [181]. The prepared HCMs had well-developed and interconnected ultrathin 3D frameworks with uniform distribution of nanopores (Figure 1.18c,d). This structure provides high surface area to physically block iodine species and fast ion transportation channels. As a result,

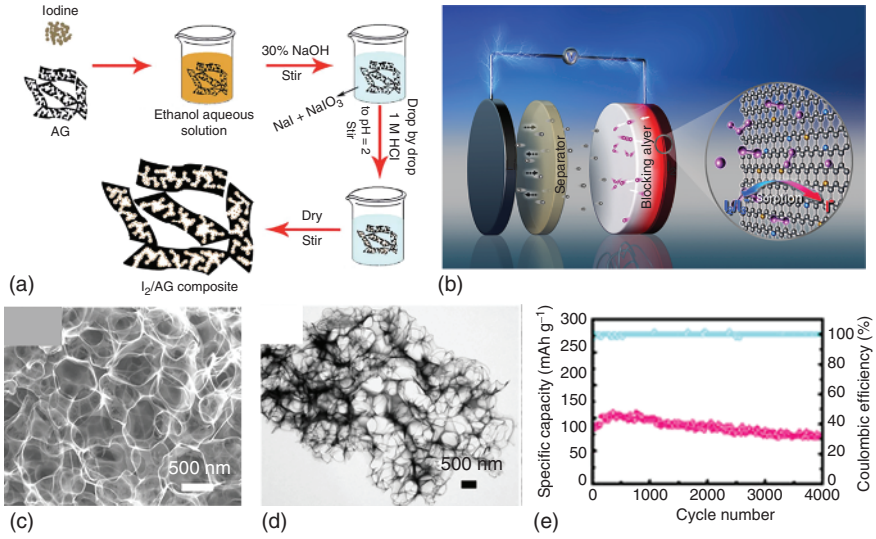

Figure 1.18 (a) Schematic depicting the in situ deposition route for fabricating the I_2-AG composites. Source: Reproduced with permission Zhang et al. [180]. (b) illustration of the working mechanism of the blocking layer in a rechargeable Li-I_2 battery; (c) SEM and (d) TEM images of synthesized HCM-5; (e) cycling performance of the as-constructed Li-I_2 batteries with HCM-5 blocking layer at a rate of 50 C. Source: Su et al. [181] / with permission of John Wiley and Sons.

the as-prepared Li–I_2 battery delivered a high capacity of 120.2 mAh g^{-1} after 4000 cycles even at a high 50 C rate (Figure 1.18e).

It is known that the reaction between nonpolar carbon and polar iodine species is poor, which is not enough to adsorb them. Thus, introducing polar functional groups into carbon matrixes is a promising way to further improve cycling stability of Li–I_2 batteries, such as heteroatom doping to increase surface polarity. Zhang's group prepared a self-standing nitrogen, phosphorus codoped carbon cloth used as a host for LiI material (Figure 1.19a) [184]. Heteroatom doping can provide extra active sites for strong adsorption of iodine species and the carbon scaffolds have abundant hierarchical pores leading to high surface area and contributing to capacity through capacitive effect (Figure 1.19b,c). These merits bring high flexibility and reversibility to Li–I_2 batteries, delivering a high capacity of 386 mAh g^{-1} while retaining 84.5% capacity after 2000 cycles. Apart from carbonaceous materials, metal-based materials were used to chemically adsorb soluble iodine species to improve the cycling stability of metal-I_2 batteries [186]. Lai's group applied a $Ti_3C_2T_x$ MXene foam as a highly effective interface layer for Li–I_2 batteries (Figure 1.19d) [185]. SEM images indicate that the prepared $Ti_3C_2T_x$ MXene exhibits a loose structure comprising ultrathin sheets, providing rich active sites to adsorb iodine species (Figure 1.19e). The thickness of $Ti_3C_2T_x$ MXene foam is about 120 μm, which is thick enough to block the transportation of soluble iodine species (Figure 1.19f). In addition, theoretical calculations revealed that the abundant functional groups on the surface of $Ti_3C_2T_x$ MXene sheets provide strong chemical

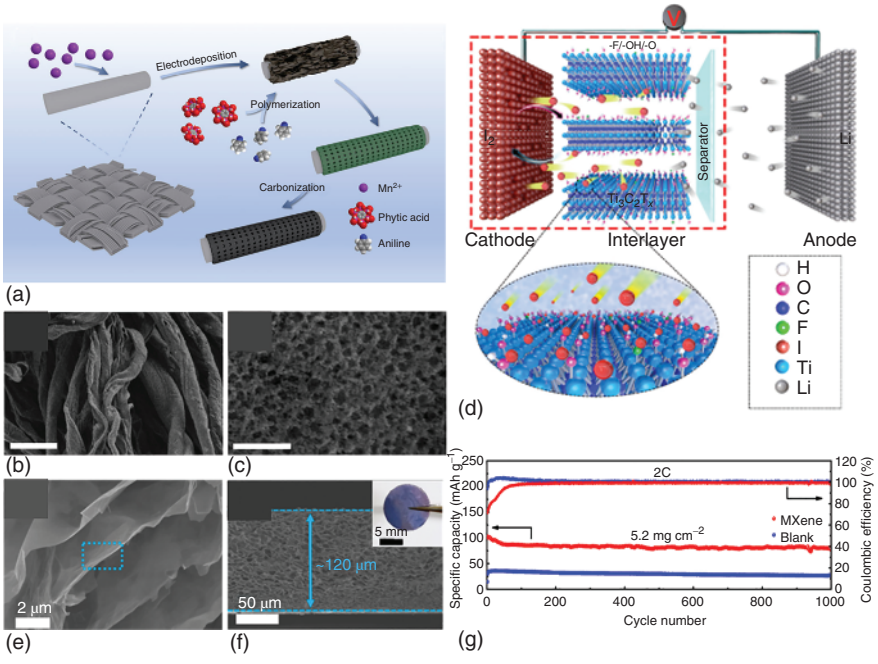

Figure 1.19 (a) Schematic illustration for the preparation process of CC-NP; (b) and (c) SEM images of CC-NP. Source: Li et al. [184]. Reproduced with permission of (2019) Springer. (d) Schematic of the reaction mechanisms of a Li-I_2 battery with a MXene interface layer; (e) SEM image of $Ti_3C_2T_x$ MXene sheets; (f) the cross-sectional SEM images of $Ti_3C_2T_x$ MXene interface layer with an inset showing a digital photo of the $Ti_3C_2T_x$ MXene interface layer; (g) long-term cycling performance and the corresponding coulombic efficiency of I_2 cathode at a mass loading of 5.2 mg cm^{-2}. Source: Sun et al. [185]. Reproduced with permission of (2020) American Chemical Society.

binding to iodine species, suppressing the shuttle effect. Moreover, high electronic conductivity of $Ti_3C_2T_x$ MXene sheets facilitates fast iodine redox reactions. As a result, the Li–I_2 battery with I_2@N-doped graphene composite cathode containing 70% I_2 and $Ti_3C_2T_x$ MXene foam as interlayer can cycle stably for over 1000 cycles at a rate of 2 C, even at an ultrahigh loading mass of 5.2 mg cm^{-2} (Figure 1.19g).

1.2.4.1.3 Anode Protection of Li–I_2 Batteries

Lithium dendrites caused by unstable SEI and the nonuniform deposition of Li ions on Li metal anodes is another challenge for practical applications of Li–I_2 batteries [187, 188]. To address this issue, Zhang's group synthesized an N, P codoped carbon (NPCC) skeleton by interfacial polymerization of polyaniline on the carbon cloth (Figure 1.20a) [189]. Then, molten lithium was loaded on the surface of 3D modified carbon cloth. The surface of prepared NPCC showed interconnected carbon nanorod networks (Figure 1.20b), indicating the successful modification of heteroatoms. In addition, the N and P elements were uniformly distributed on the surface of NPCC (Figure 1.20c), leading to a lithiophilic surface to uniformly load Li

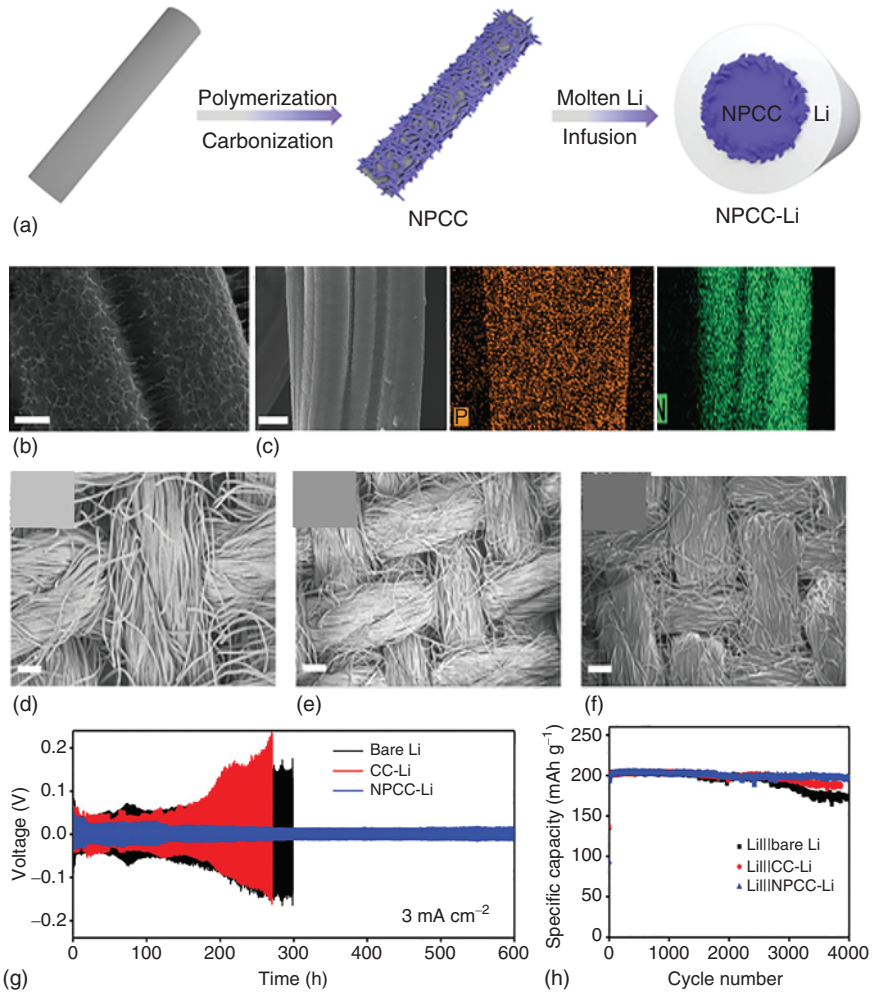

Figure 1.20 (a) Schematic illustration of the synthesis process of NPCC-Li; (b) SEM images of NPCC; (c) uniform distribution of N and P on NPCC; SEM images of NPCC with different Li loading: (d) 3.5, (e) 7.5, and (f) 12 mg; (g) galvanostatic charge–discharge curves of symmetric cells assembled with Li, CC-Li, and NPCC-Li electrodes at current density 3 mA cm^{-2}; (h) cycling performances of full cells with iodine cathode. Source: Li et al. [189] / with permission of John Wiley and Sons.

metal. Due to the uniform, lithiophilic surface, the Li metal can be uniformly coated on the carbon skeleton, even with a high mass loading of 12 mg cm^{-2} without any agglomeration (Figure 1.20d–f). Moreover, the 3D porous structure formed would lower the local current density for reversible deposition and stripping of Li metal. The Li symmetric cells could stably cycle for over 600 hours at a current density of 3 mA cm^{-2} (Figure 1.20g). When coupled with iodine cathode, the assembled battery showed an impressive long-term cycling stability with a capacity retention of 99% after 4000 cycles (Figure 1.20h).

In summary, modification of carbon materials with heteroatom doping or adding metal-based materials could enhance physical and chemical adsorption between iodine and carbon substrates, leading to long, stable cycling performance. Designing carbon materials with ultrahigh surface area will lead to higher specific capacity at a high scan rate due to the capacitive effect offered by carbon materials. Additionally, the lithium dendrites need to be inhibited to promote practical applications of Li–I_2 batteries. Fabricating 3D lithium anode is a useful way verified by researchers. Some more strategies can be designed, such as applying electrolyte additives, forming stable artificial SEI layer. If all these problems can be solved, the commercialization of Li–I_2 batteries with high energy density is not far.

1.2.4.2 Lithium–Bromine Battery

In comparison with iodine, bromine as a liquid at room temperature makes it more difficult to fabricate batteries. Due to its stable and high redox potential (1.05 V vs. SHE), good reversibility, fast kinetics, and high solubility in water, bromine was investigated in redox flow cell, such as Zn–Br batteries [190].

In 2014, a Li//Br battery was designed by Yu's group [191]. The aqueous LiBr solution was used as electrolyte, with liquid Br_2 or Br^{3-} as the positive electrode and glassy carbon as the current collector. Lithium metal was coated with a home-made gel polymer electrolyte (GPE) and a ceramic solid electrolyte (LISICON) film, as shown in Figure 1.21a. The redox reactions of the designed Li//Br battery are given as follows:

$$\text{Oncathode side}: 2Li + Br_3^- \leftrightarrow 3Br^- + 2Li^+$$

$$\text{On anode side}: Li \leftrightarrow Li^+ + e^-$$

Br^-/Br_3^- redox reaction provides the Li//Br battery with a high energy density of 1220 Wh kg^{-1}, a power density of 29.7 mW cm^{-2} at a current density of 12.8 mA cm^{-2}, and a long cycling life. In addition, discharge voltage of the battery

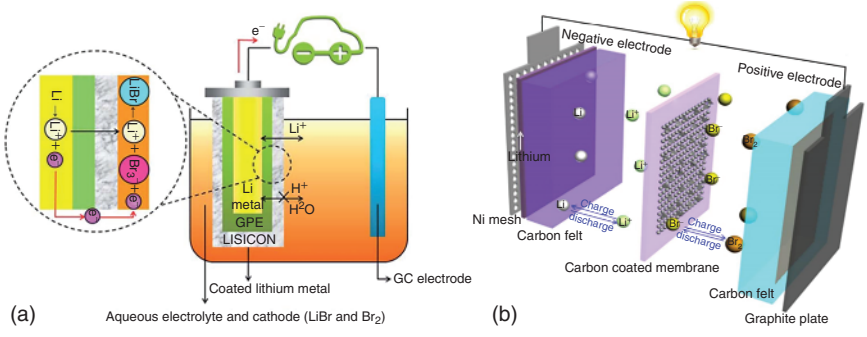

Figure 1.21 (a) Schematic illustration of our rechargeable Li//Br battery composed of Li metal coated with GPE and LISICON as the negative electrode, aqueous LiBr solution (1 M) as the electrolyte, and 0.1 M liquid Br_2 or Br_3^- as the positive electrode with glassy carbon as the current collector. Source: Reproduced with permission Chang et al. [191].
(b) Schematic illustration of a nonaqueous Li/Br battery. Source: Reproduced with permission Xi et al. [192].

is high (3.96 V) and very stable, without degradation during the discharge process. These advantages enable Li/Br batteries competitive to commercial Li–ion batteries. Recently, a nonaqueous lithium bromine rechargeable battery is proposed by Zhang's group [192]. On the Li metal anode side, Ni mesh was used as current collector and carbon felt was used to carry the electrolyte. On the cathode side, graphite plate was applied as the current collector and carbon felt was used to adsorb the electrolyte. The electrolyte consisted of 2 M LiBr in 1.3 M LiTFSI DOL/DME solution. A carbon-coated membrane was applied as a separator (Figure 1.21b). The designed Li–Br batteries operated via the redox conversion of Br_2/Br^- and Li^+/Li pairs, as follows:

$$\text{Cathode side}: Br_2 + 2e^- \leftrightarrow 2Br^-$$

$$\text{Anode side}: Li - e^- \leftrightarrow Li^+$$

Fast redox kinetics and good stability of Br_2/Br^- offer the Li/Br battery with high output voltage (~3.1 V), high electrolyte concentration (3.0 M), and practical energy density (232.6 Wh kg^{-1}). The nonaqueous Li/Br battery can be readily scaled up as alternatives of Li-ion batteries.

Although great achievements have been made on Li–Br batteries, compared with Li–I_2 batteries, the research on Li–Br batteries are limited due to the liquid state of Br_2 at room temperature. To find stable supporters or host materials for Br_2 at room temperature is a big challenge with Li–Br_2 batteries. Although high energy density is achieved, specific capacity of Li–Br batteries is ultralow. Adding redox pairs, such as Cl/Cl^- with a theoretical capacity up to 755 mAh g^{-1} can further improve the capacity as well as energy density. Another challenge to be solved is the shuttle effect, which has not been reported in Li–Br batteries. Applying matrixes with both physical and chemical adsorption functions is a promising way. As for Li metal anodes, Li dendrites should be considered to improve the long-term stability of Li–Br batteries. The strategies already applied in other Li metal batteries can be used as reference, such as adding electrolyte additives, forming artificial SEI layer, or synthesizing 3D matrixes to load Li metal. These are alternative ways to develop advanced rechargeable Li–Br batteries with high energy density and stable reversibility.

1.2.5 TMO Batteries

The Li-ion batteries have been dominating the green energy markets for several decades, which consist of graphite as anode and lithium-containing transition metal compounds with different structures, such as olivine ($LiMPO_4$:M = transition metal), layered ($LiMO_2$), or spinel (LiM_2O_4) materials [193]. However, the state-of-the-art commercial Li-ion batteries have already reached their theoretical capacity limitation. The emergence of grids and electric vehicles drives the researchers to find electrode materials with higher capacity and energy density [194]. Li metal is thus believed to be the ultimate choice to replace graphite anodes due to its high theoretical specific capacity (3860 mAh g^{-1}) and lightweight (0.53 g cm^{-3}). For cathode materials, compared with lithium-containing transition metal oxides, lithium-free transition metal oxides (TMOs) are also considered

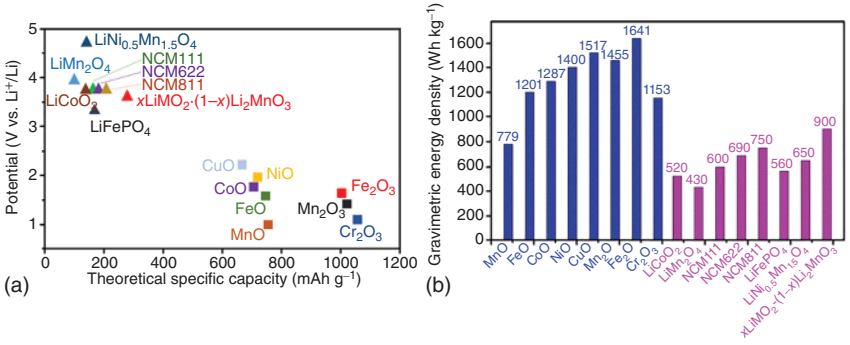

Figure 1.22 Fundamentals of conversion reaction-type TMOs. (a) Theoretical specific capacity and voltage and (b) energy density for the TMOs compared to conventional cathodes. Source: Reproduced with permission Wu et al. [196].

promising candidates [195, 196]. As shown in Figure 1.22, the TMO materials offer much higher specific capacity than that of conventional intercalation/phase transition-type cathodes such as LFP, $LiCoO_2$ (LCO), NCM, and even Li-rich Mn-based oxides. In addition, when coupled with Li metal, TMOs have the potential to offer energy density of 1200–1700 Wh kg^{-1}, which is two or three times that of commercialized cathode materials of Li–ion batteries. Although the operating voltage of TMOs is relatively lower, their high specific capacity still can yield higher energy density.

Several TMOs have been prepared as cathode materials for Li metal batteries. Deng's group prepared three kinds of conversion reaction-type TMOs (Fe_2O_3, Mn_2O_3 or CuO) as Li-free cathodes for solid-state Li metal batteries, in which PEO, lithium garnet $Li_{6.4}La_3Zr_{1.4}Ta_{0.6}O_{12}$ (LLZTO), or $Li_{1.5}Al_{0.5}Ge_{1.5}(PO_3)_4$ (LAGP) are employed as SSEs [196]. The cathodes offer good interfacial compatibility with the SSEs, leading to excellent electrochemical performance of the TMOs/SSEs/Li solid-state cells. The prepared Fe_2O_3 has a small size with nanostructures (Figure 1.23a); when used as cathode in the solid-state Li metal battery, the Fe_2O_3/PEO/Li cell delivers a high discharge capacity of 990 mAh g^{-1} at 10 mA g^{-1} at 60 °C, which is comparable to the Fe_2O_3 liquid cell. When cycling at 200 mA g^{-1} a stable capacity of 733 mAh g^{-1} is achieved after 1100 cycles for the Fe_2O_3/PEO/Li cell, while the Fe_2O_3 liquid cell sustains only 860 cycles until failure (Figure 1.23b). The MnO_2 sheets showing a high specific capacity of 616 mAh g^{-1} is regarded as a promising cathode for Li metal batteries. But the structural collapse during cycling hinders its further application. To improve the structural stability of MnO_2 nanosheets, Deng and coworkers designed a three-dimensional porous NiO nanorod pillared δ-MnO_2 nanosheets integrated nanostructure as cathode materials for Li metal batteries (Figure 1.23c) [197]. The NiO pillars not only can prevent restacking of δ-MnO_2 nanosheets but also provide more electrochemically active sites and thermodynamically favorable insertion pathways for the lithium ions. Thus, the as-synthesized NiO pillared δ-MnO_2 nanosheets delivered a relatively high specific capacity of 185 mAh g^{-1} and maintained a capacity of 116 mAh g^{-1} after 200 cycles at 100 mA g^{-1} (Figure 1.23d).

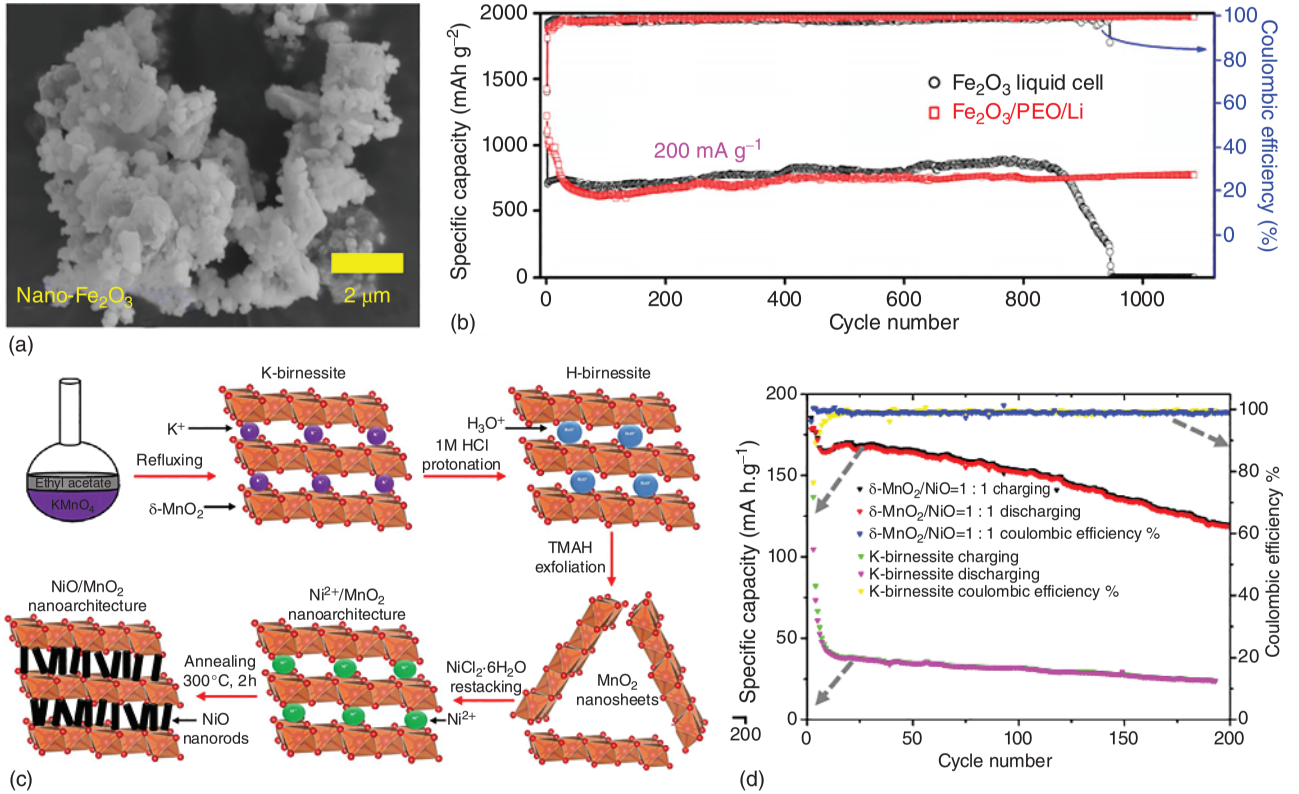

Figure 1.23 (a) SEM image of prepared nano-Fe_2O_3 and (b) cycling performance of Fe_2O_3/PEO/Li and Fe_2O_3 liquid cells for 1100 cycles at 200 mA g^{-1}. Source: Wu et al. [196] / with permission from Elsevier. (c) Schematic showing the steps and structural changes involved in the synthesis of 3-D nanoarchitectures of NiO nanorod pillared δ-MnO_2 nanosheets; (d) cycling performance of δ-MnO_2 nanosheets and NiO pillared δ-MnO_2 nanosheets as lithium-free cathode materials at 100 mA g^{-1}. Source: Reproduced with permission Hewavitharana et al. [197].

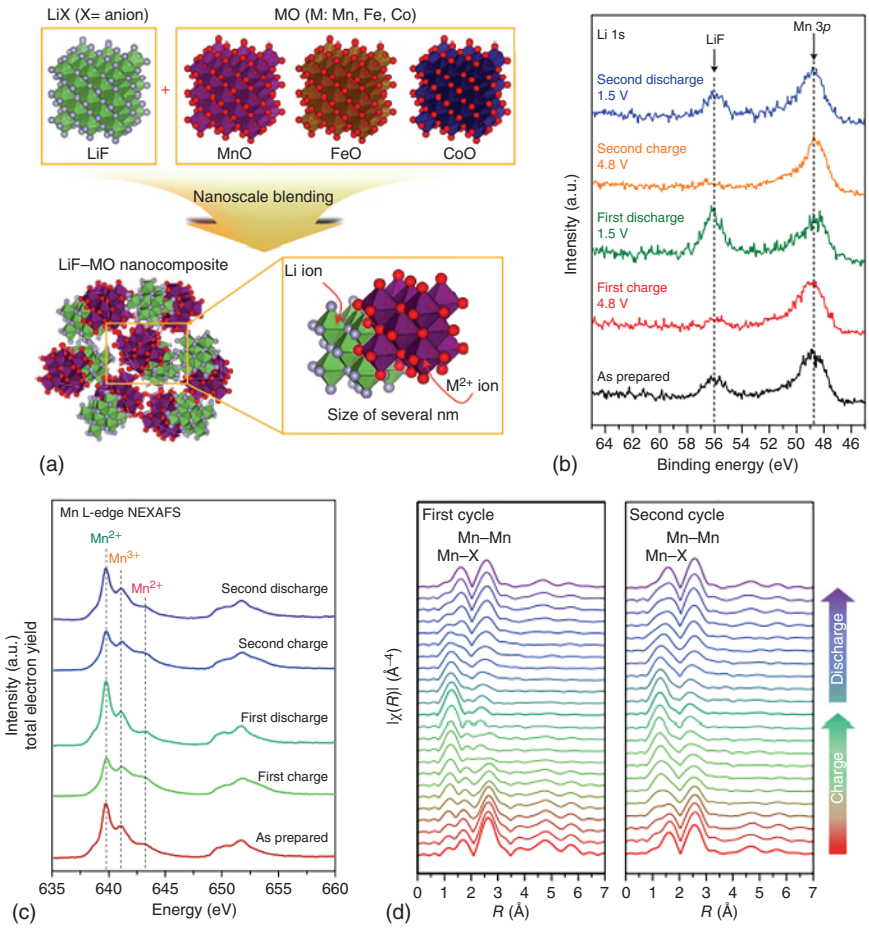

Figure 1.24 (a) Schematic of the positive electrode material design strategy using metal monoxide (MO); (b) ex situ XPS spectra of Li 1s, including the range of Mn 3p binding energy; (c) Mn L-edge NEXAFS spectra of the LiF–MnO nanocomposite from total electron yield mode with different electrochemical states; (d) in situ EXAFS spectra during two cycles in the 1.5–4.8 V range. Source: Reproduced with permission Jung et al. [198].

Except pure TMOs, LiF was applied on TMOs to improve the operating voltage. In 2017, Kang's group synthesized LiF/MnO composites via high-energy ball-milling method (Figure 1.24a) [198]. There is no chemical reaction between MnO and LiF. To understand the role of LiF during discharge/charge process, the Li 1s region was analyzed by XPS, as shown in Figure 1.24b. The signal of LiF at 56.0 eV disappeared at charge and recovered at discharge, indicating the F ion can be bound to the Mn ion to satisfy charge neutrality when oxidation occurs. To further reveal the electrochemical reaction between the MnO and F ions, further analysis was done by soft X-ray absorption spectroscopy (Figure 1.24c). On charging, the Mn^{3+} and Mn^{4+} signals increased at the expense of the Mn^{2+} signal. The reversible change was observed during the subsequent electrochemical cycling, which indicates that

not only Mn^{2+}/Mn^{3+} but also Mn^{3+}/Mn^{4+} redox reactions are involved in the electrochemical reaction. To observe the local structure evolution, extended X-ray absorption fine structure (EXAFS) analysis was used, indicating that the structural transition is reversible during electrochemical cycling. Therefore, the reaction mechanism of the LiF/MnO nanocomposite can be called a "surface conversion reaction," which is described as follows:

$$LiF + Mn^{2+}O \rightarrow Li^{+} + e^{-} + Mn^{3+}O\text{–}F$$

LiF functions not only as a Li source for cathode materials but also as an anion source for charge compensation when oxidation and reduction of a transition metal ion occur. LiF can be regarded as a stabilizer of the oxidized Mn^{3+} (or Mn^{4+}) ion by providing F^{-} ions from the MnO perspective. In addition, the MnO can be regarded as an assistant that promotes the decomposition of LiF. As a result, the LiF/MnO composites exhibit an average voltage of over 3 V (vs. Li^{+}/Li).

Although some TMOs have been studied as cathode materials for Li metal batteries, compared with metal sulfides or fluorides, the development of TMOs is still in its infant stage. There are some problems that need to be addressed to promote the application of TMOs. First, the cycling stability of TMOs in liquid Li metal batteries is inferior. The mechanism and strategies should be developed, such as applying in situ analysis techniques and surface coating. The rate capability of TMOs in solid-state Li metal batteries should be improved by synthesizing SSEs with high ionic conductivity.

1.3 Introductive Electrolytes

Li metal has been intensively investigated as anode due to its ultrahigh theoretical specific capacity (3860 mAh g^{-1}) and the most negative electrochemical potential (~3.040 V vs. SHE). When paired with cathode materials, Li metal batteries can deliver higher capacity and higher operating voltage, leading to higher energy density, which make lithium metal batteries (LMBs) promising power devices for long-term vehicles or large-scale grids to replace commercial Li-ion batteries [199]. Despite of these advantages, several problems are also found that hinder practical applications of LMBs [200]. As shown in Figure 1.25a, the Li metal can react with the electrolyte to form an SEI layer on the surface of the Li metal anode. During plating process, volume expansion will occur, which can crack the unstable SEI layer. The new exposed Li metal will form dendrites. In the subsequent striping process, the dendrite-like Li metal will be isolated to form "dead" Li. During the long-term cycling process, a porous Li metal with thick SEI and accumulated dead Li will be obtained, which can lead to low columbic efficiency, capacity fading, and failure of cells. To overcome these concerns, various approaches have been reported in the literature to make Li metal anodes with high stability, including electrolyte formulation [202], SSEs [203], artificial stable SEI [204], and anode structure design [205]. Among them, electrolytes play a vital role in obtaining a mechanical stable SEI layer and suppressing the growth of Li dendrites [201, 206, 207].

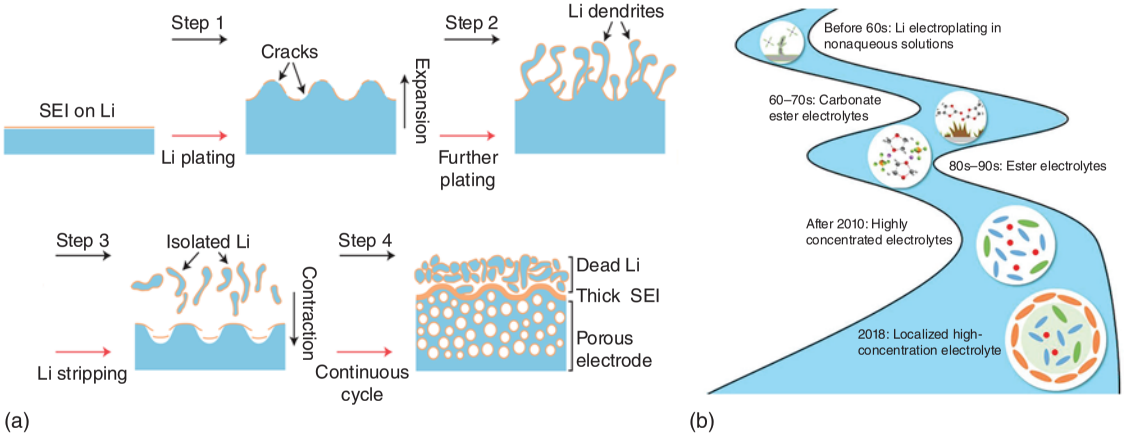

Figure 1.25 (a) Schematic showing the problems related to Li metal during the Li stripping/plating process. Source: Reproduced with permission Lin et al. [200]. (b) Schematic diagram for the development progress of liquid electrolytes in lithium metal batteries. Source: Reproduced with permission Jie et al. [201].

As shown in Figure 1.25b, the investigation of electrolyte for Li plating/striping can be dated back to the nineteenth century, using a nonaqueous electrolyte with LiCl and pyridine. Then, different salts and solvents were studied [208, 209]. After preliminary studies, aprotic solvents were proved to be useful to inhibit the reaction between Li metal and electrolytes. In the 1960s, due to the demand for high-energy-density storage systems, the electrolytes used in LMBs started to get attention. Electrolytes with alkyl carbonate esters such as propylene carbonate (PC) as solvents and $LiPF_6$ or $LiClO_4$ as Li salts were used in rechargeable batteries due to their good ionic conductivity [210]. However, carbonate ester-based electrolytes showed low coulombic efficiency, which hindered their further application [211].

In the late 1970s, ether electrolytes were reported, which could obtain high CE and stable reversibility of the Li electrode due to the formation of more suitable SEI layers with both organic and inorganic contents [212]. With the commercialization of Li–ion batteries with graphite as anode, the research on electrolytes for LMBs was limited. Recently, as graphite anodes are approaching their theoretical capacity, there has been a renaissance in LMBs. At this stage, excellent strategies have been applied to improve the cycling stability of both anode and cathode through electrolyte modifications. Adding suitable electrolyte additives is a simple and promising way to in situ form stable solid electrolyte interfaces on both anode and cathode, leading to enhanced cycling stability of LMBs [213]. For example, gradient SEI layer was formed by adding bisfluoroacetamide (BFA) into the electrolyte, consisting of a C–F rich surface and a LiF rich bottom layer (Figure 1.26a,b), which can contribute to the preferential reduction of BFA on Li metal surface due to higher reductive potentials (Figure 1.26c) [214]. As a result, the Li||Li batteries can stably cycle for 400 cycles at a current density of $1\,mA\,cm^{-1}$ (Figure 1.26d). The solvation structures of Li ions can also be changed by adding electrolyte additives, such as alkyl-triphenyl-phosphonium bromides (alkyl-TPPB) [215]. The presence of Br^- ions in the electrolyte can enlarge the reaction distance between Li ions with solvents (Figure 1.26e). Thus, the coordinate number of EC in solvation structures decreases, which can suppress the reduction of solvents and improve the stability of electrolytes. HCEs were also reported to improve the cycling stability of Li metal anodes [216, 217]. In addition, HCEs exhibit good oxidation stability, which can simultaneously improve the stability of cathode materials, such as $LiNi_{0.8}Mn_{0.1}Co_{0.1}O_2$ (NMC811). However, high cost and viscosity of HCEs make them unsuitable for practical applications. Therefore, diluents are added into electrolytes to form localized high-concentration electrolytes (LHCEs) [218]. LHCEs exhibit the advantages of HCEs, as well as decrease the cost and viscosity of HCEs, which are regarded as advanced liquid electrolytes for Li metal batteries.

Except these electrolyte modifications, some functional electrolytes were also studied, such as nonflammable electrolytes [219], high-voltage electrolytes [220], electrolytes operated at extreme conditions (such as high or low temperature) [221]. Significant advances from both the fundamental understanding and practical engineering have been made, but the reaction between Li metal and electrolyte is

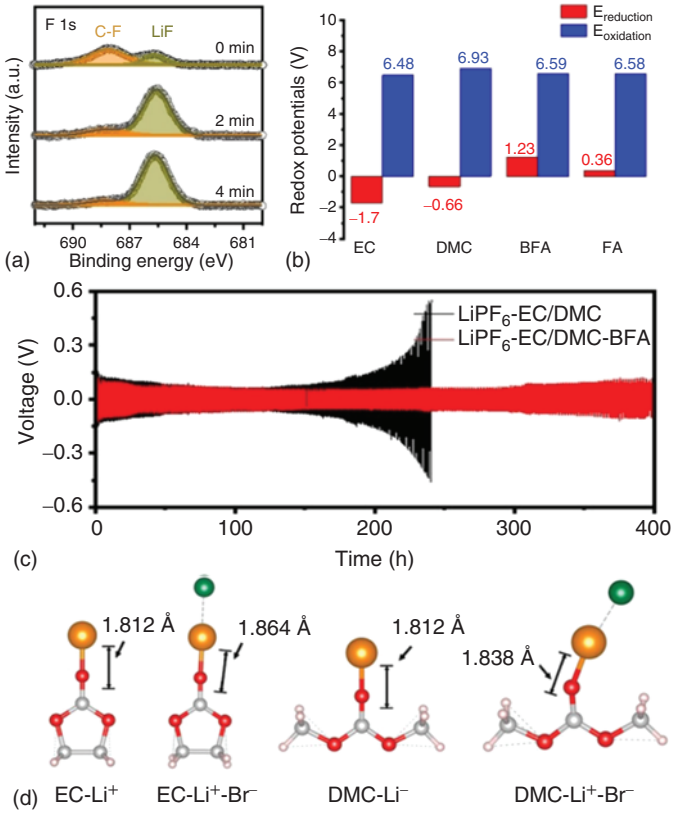

Figure 1.26 (a) XPS spectra of F 1s in Li||Li cells after 10 cycles in $LiPF_6$-EC/DMC-BFA electrolyte. (b) Theoretical calculation of redox potentials of EC, DMC, BFA, and FA molecules; (c) cycling performance of Li||Li cells using $LiPF_6$-EC/DMC-BFA electrolyte at a current density of 1 mA cm^{-2} with a cutoff capacity of 0.5 mAh cm^{-2}. Source: Reproduced with permission Li et al. [214]. (d) The comparison of the distance between Li^+ ion and O atom of the EC and DMC molecules with and without the Br^- ion coordinator. Source: Reproduced with permission Qi et al. [215].

not inhibited, which will affect the practical applications of LMBs with long-term requirements.

1.4 Prospects

Over the past several decades, LMBs have been regaining intensive research attention due to their high energy density compared with Li-ion batteries. Until now, practical applications of LMBs with different cathodes is not realized due to their inherent drawbacks. Therefore, to solve these detrimental issues and realize the practical deployment of LMBs, many problems need to be addressed:

(1) Mechanism: Clear understanding of the reaction mechanism is vital to further improve electrochemical performance of batteries. The mechanism of Li_2O_2

decomposition on a cathode catalyst in Li–O_2 batteries is not elucidated yet. Due to the sluggish kinetics of O_2, designing cathodes with high surface area as well as catalysts with high OER catalytic activity is important. In addition, for practical applications of Li–O_2 batteries, the effect of CO_2 in air should be considered, which can react with Li_2O_2 to produce Li_2CO_3. For Se cathodes, the redox reaction pathway in carbonate electrolytes is not clear. Some works indicate a single-conversion process, while others indicate a multiple-reaction process. In addition, due to the insolubility of polyselenides in carbonate electrolytes, in-depth research needs to be done on carbonate electrolytes rather ether-based electrolytes.

(2) Shuttle effect: The shuttle effect is a big problem in Li–S, Li–Se/Te, Li–I_2/Br_2 batteries. To solve this problem, designing cathode host materials with both physical and chemical adsorption properties is a promising way, such as heteroatom doping on carbonaceous materials and introducing metal-based polar species. Inserting a block interlayer is the simplest way. For practical applications, lean electrolytes and high mass loading should be considered, which are generally are paid less attention. Exploring SSEs with high ionic conductivity is the direct way to inhibit the shuttle effect.

(3) Li metal anodes: Due to random deposition of Li ions, the dendrite growth is the biggest challenge with Li metal batteries. More works on anode protection need to be done, such as electrolyte additives, SSEs, or artificial SEI layer on Li metal. To further understand anode and electrolyte degradation as well as the components and structures of electrolyte interfaces, new analytical tools and in situ techniques should be applied.

If these problems are solved, Li metal batteries will take great strides toward their practical applications.

References

1 Wu, X., Wang, J., Fei, D. et al. (2014). *Energy & Environmental Science* 7 (2): 513–537.

2 Lin, D., Liu, Y., and Yi, C. (2017). *Nature Nanotechnology* 12 (3): 194–206.

3 Whittingham, M.S. (2004). *Chemical Reviews* 35 (50): 4271–4301.

4 Dusastre, V. (2011). *Materials for Sustainable Energy*. Nature Publishing Group.

5 Hong, L., Wang, Z., Chen, L., and Huang, X. (2009). *Advanced Materials* 21 (45): 4593–4607.

6 Li, M., Lu, J., Chen, Z., and Amine, K. (2018). *Advanced Materials* 30 (33): *1800561*.

7 Daniel, I.C. and Besenhard, J.O. (2012). *Handbook of Battery Materials*, 2e. John Wiley & Sons.

8 Chen, L., Liu, Y., Ashuri, M. et al. (2014). *Journal of Materials Chemistry A* 2 (42): 18026–18032.

9 Reich, H.J., Bevan, M.J., Gudmundsson, B., and Puckett, C.L. (2002). *Angewandte Chemie International Edition* 41 (18): 3436–3439.

10 Sun, J., Du, Z., Liu, Y. et al. (2021). *Advanced Materials* 33 (10): 2003845.
11 Lu, J., Li, L., Park, J.B. et al. (2014). *Chemical Reviews* 114 (11): 5611–5640.
12 Lu, K., Hu, Z., Ma, J. et al. (2017). *Nature Communications* 8 (1): 1–10.
13 Xu, J., Ma, J., Fan, Q. et al. (2017). *Advanced Materials* 29 (28): 1606454.
14 Cheng, X.B., Zhang, R., Zhao, C.Z., and Zhang, Q. (2017). *Chemical Reviews* 117 (15): 10403–10473.
15 Shao, Y., Fei, D., Jie, X. et al. (2013). *Advanced Functional Materials* 23 (8): 987–1004.
16 Kwak, W., Rosy, D., Sharon, C. et al. (2020). *Chemical Reviews* 120 (14): 6626–6683.
17 Lyu, Z., Zhou, Y., Dai, W. et al. (2017). *Chemical Society Reviews* 46 (19): 6046–6072.
18 Yu, Z., Wang, H., Kong, X. et al. (2020). *Nature Energy* 5: 526–533.
19 Lim, H.K., Lim, H.D., Park, K.Y. et al. (2013). *Journal of the American Chemical Society* 135 (26): 9733–9742.
20 McCloskey, B.D., Bethune, D.S., Shelby, R.M. et al. (2011). *Journal of Physical Chemistry Letters* 2 (10): 1161–1166.
21 McCloskey, B.D., Speidel, A., Scheffler, R. et al. (2012). *Journal of Physical Chemistry Letters* 3 (8): 997–1001.
22 McCloskey, B.D., Scheffler, R., Speidel, A. et al. (2011). *Journal of the American Chemical Society* 133: 18038.
23 Chang, Z., Xu, J., and Zhang, X. (2017). *Advanced Energy Materials* 7 (23): 1700875.
24 Wang, D., Mu, X., He, P., and Zhou, H. (2019). *Materials Today* 26: 87–99.
25 Xiao, J., Mei, D., Li, X. et al. (2011). *Nano Letters* 11 (11): 5071–5078.
26 Jiao, W., Su, Q., Ge, J. et al. (2021). *Materials Research Bulletin* 133: 111020.
27 Huang, H., Luo, S., Liu, C. et al. (2017). *Journal of Alloys and Compounds* 726: 939–946.
28 Jung, J.-W., Choi, D.-W., Lee, C.K. et al. (2018). *Nano Energy* 46: 193–202.
29 Kim, M., Kim, D.W., Suk, J. et al. (2015). *Carbon* 93: 625–635.
30 Chang, Y., Dong, S., Ju, Y. et al. (2015). *Advanced Science* 2 (8): 1500092.
31 Cao, Y., Lu, H., Hong, Q. et al. (2019). *Carbon* 144: 280–288.
32 Nie, H., Xu, C., Zhou, W. et al. (2016). *ACS Applied Materials & Interfaces* 8 (3): 1937–1942.
33 Cao, D., Zhang, S., Yu, F. et al. (2019). *Batteries & Supercaps* 2 (5): 428–439.
34 Zhao, Y., Ding, L., Wang, X. et al. (2021). *Journal of Alloys and Compounds* 861: 157945.
35 Luo, N., Ji, G.-J., Wang, H.-F. et al. (2020). *ACS Nano* 14 (3): 3281–3289.
36 Shui, J.-L., Okasinski, J.S., Kenesei, P. et al. (2013). *Nature Communications* 4 (1): 1–7.
37 Zhang, X., Xie, Z., and Zhou, Z. (2019). *ChemElectroChem* 6 (7): 1969–1977.
38 Ko, J. and Yoon, Y.S. (2018). *Ceramics International* 45 (1): 30–49.
39 Yu, Y., Huang, G., Wang, J.Z. et al. (2020). *Advanced Materials* 32 (38): 2004157.
40 Adair, K.R., Zhao, C., Banis, M.N. et al. (2019). *Angewandte Chemie International Edition* 58 (44): 15797–15802.

41 Luo, Z., Zhu, G., Yin, L. et al. (2020). *ACS Applied Materials & Interfaces* 12 (24): 27316–27326.

42 Yu, Y., Yin, Y.-B., Ma, J.-L. et al. (2019). *Energy Storage Materials* 18: 382–388.

43 Liu, T., Leskes, M., Yu, W. et al. (2015). *Science* 350: 530–533.

44 Yang, L., Wang, X., Dong, S. et al. (2016). *Advanced Energy Materials* 6 (18): 1600751.

45 Yu, Y. and Zhang, X.-B. (2019). *Matter* 1 (4): 881–892.

46 Liu, B., Xu, W., Yan, P. et al. (2016). *Advanced Functional Materials* 26 (4): 605–613.

47 Wu, S., Zhu, K., Tang, J. et al. (2016). *Energy & Environmental Science* 9 (10): 3262–3271.

48 Qin, L., Zhai, D.Y., Lv, W. et al. (2017). *Nano Energy* 40: 258–263.

49 Manthiram, A., Fu, Y., Chung, S.-H. et al. (2014). *Chemical Reviews* 114 (23): 11751–11787.

50 Ruopian, F., Shiyong, Z., Zhenhua, S. et al. (2017). *Advanced Materials* 29 (48): *1606823*.

51 He, J. and Manthiram, A. (2020). *Advanced Energy Materials* 10 (3): 1903241.

52 Danuta, H.; Juliusz, U. (1962). Electric dry cells and storage batteries. U.S. Patent, No.3,043,896.

53 Rauh, R.; Pearson, G.; Brummer, S. (1977). *Rechargeability studies of ambient temperature lithium/sulfur batteries*. 12th Intersociety Energy Conversion Engineering Conference, American Nuclear Society, 1, 283–287.

54 Linden, D. and McDonald, B. (1980). *Journal of Power Sources* 5 (1): 35–55.

55 Yamin, H., Gorenshtein, A., Penciner, J. et al. (1988). *Journal of the Electrochemical Society* 135 (5): 1045.

56 Wang, J., Yang, J., Xie, J., and Xu, N. (2002). *Advanced Materials* 14 (13–14): 963–965.

57 Fu, C. and Guo, J. (2016). *Current Opinion in Chemical Engineering* 13: 53–62.

58 Eftekhari, A. and Kim, D.-W. (2017). *Journal of Materials Chemistry A* 5 (34): 17734–17776.

59 Deng, N., Kang, W., Liu, Y. et al. (2016). *Journal of Power Sources* 331: 132–155.

60 Jin, Z., Kai, X., and Hong, X. (2014). *Acta Chimica Sinica* 72 (1): 11.

61 Peled, E., Gorenshtein, A., Segal, M., and Sternberg, Y. (1989). *Journal of Power Sources* 26: 269–271.

62 Xiulei, J., Kyu, T., Lee, N., and Linda, F. (2009). *Nature Materials* 8 (6): 500–506.

63 Xin, S., Gu, L., Zhao, N.H. et al. (2012). *Journal of the American Chemical Society* 134 (45): 18510–18513.

64 Papandrea, B., Xu, X., Xu, Y. et al. (2016). *Nano Research* 9 (1): 240–248.

65 Lee, J.S., Kim, W., Jang, J., and Manthiram, A. (2017). *Advanced Energy Materials* 7 (5): 1601943.

66 Liang, J., Sun, Z.-H., Li, F., and Cheng, H.-M. (2016). *Energy Storage Materials* 2: 76–106.

67 Li, S., Bo, J., Zhai, X. et al. (2018). *ChemistrySelect* 3 (8): 2245–2260.

68 Tang, Q., Li, H., Zuo, M. et al. (2017). *Nano* 12 (2): 1750021.

69 Yu, M., Li, R., Wu, M., and Shi, G. (2015). *Energy Storage Materials* 1: 51–73.
70 Schipper, F., Vizintin, A., Ren, J. et al. (2015). *ChemSusChem* 8 (18): 3077–3083.
71 Li, X. (2014). *Frontiers in Energy Research* 2: 1.
72 Wu, D., Liu, J., Chen, J. et al. (2021). *Journal of Materials Chemistry A* 9: 5497–5506.
73 Ramakumar, S., Dasari, B., Ramesha, K., and Karkera, G. (2021). *Energy & Fuels* 35 (9): 8286–8294.
74 Hou, T.Z., Chen, X., Peng, H.J. et al. (2016). *Small* 12: 3283–3291.
75 Salem, H.A., Babu, G., Rao, C.V., and Arava, L. (2015). *Journal of the American Chemical Society* 137 (36): 11542.
76 Deng, C., Wang, Z., Feng, L. et al. (2020). *Journal of Materials Chemistry A* 8: 19704–19728.
77 Yu, M., Zhou, S., Wang, Z. et al. (2019). *Energy Storage Materials* 20: 98–107.
78 Song, Y., Cai, W., Kong, L. et al. (2020). *Advanced Energy Materials* 10 (11): 1901075.
79 Hong, X., Wang, R., Liu, Y. et al. (2020). *Journal of Energy Chemistry* 42: 144–168.
80 Yang, D.D., Hong, P.D., Hu, Y. et al. (2021). *Applied Surface Science* 552: 149424.
81 He, J., Bhargav, A., Asl, H.Y. et al. (2020). *Advanced Energy Materials* 10 (23): 2001017.
82 Wu, Y., Zhu, X., Li, P. et al. (2019). *Nano Energy* 59: 636–643.
83 Wu, H., Jiang, H., Yang, Y. et al. (2020). *Journal of Materials Chemistry A* 8 (29): 14498–14505.
84 Xia, G., Zheng, Z., Ye, J. et al. (2020). *Chemical Engineering Journal* 406: 126823.
85 Ye, Z., Jiang, Y., Li, L. et al. (2020). *Advanced Materials* 32 (32): 2002168.
86 Shi, Z., Sun, Z., Cai, J. et al. (2020). *Advanced Functional Materials* 31 (4): 2006798.
87 Wang, F., Li, J., Zhao, J. et al. (2020). *ACS Materials Letters* 2 (11): 1450–1463.
88 Zhou, G., Tian, H., Yang, J. et al. (2017). *Proceedings of the National Academy of Sciences of the United States of America* 114 (5): 840.
89 Lu, Y., Tu, Z., Shu, J., and Archer, L.A. (2015). *Journal of Power Sources* 279: 413–418.
90 Su, Y.-S. and Manthiram, A. (2012). *Nature Communications* 3 (1): 1–6.
91 Li, Z., Tang, L., Liu, X. et al. (2019). *Electrochimica Acta* 310: 1–12.
92 Song, Y., Zhao, S., Chen, Y. et al. (2019). *ACS Applied Materials & Interfaces* 11 (6): 5687–5694.
93 Han, P. and Manthiram, A. (2017). *Journal of Power Sources* 369: 87–94.
94 Gu, S., Sun, C., Xu, D. et al. (2018). *Electrochemical Energy Reviews* 1 (4): 599–624.
95 Gu, S., Qian, R., Jin, J. et al. (2016). *Physical Chemistry Chemical Physics* 18 (42): 29293–29299.
96 Xu, R.-c., Xia, X.-h., Wang, X.-l. et al. (2017). *Journal of Materials Chemistry A* 5 (6): 2829–2834.

97 Unemoto, A., Yasaku, S., Nogami, G. et al. (2014). *Applied Physics Letters* 105 (8): 083901.

98 Lau, K.C., Rago, N., and Chen, L. (2019). *Journal of the Electrochemical Society* 166 (12): A2570–A2573.

99 Fan, L.L., Deng, N.P., Yan, J. et al. (2019). *Chemical Engineering Journal* 369: 874–897.

100 Zhang, S., Ueno, K., Dokko, K., and Watanabe, M. (2015). *Advanced Energy Materials* 5 (16): 1500117.

101 Judez, X., Martinez-Ibanez, M., Santiago, A. et al. (2019). *Journal of Power Sources* 438: 226981–226985.

102 Yue, J., Yan, M., Yin, Y.X., and Guo, Y.G. (2018). *Advanced Functional Materials* 28 (38): 1707533.

103 Liu, Y., He, P., and Zhou, H. (2018). *Advanced Energy Materials* 8 (4): 1701602.

104 Camacho-Forero, L.E., Smith, T.W., Bertolini, S., and Balbuena, P.B. (2015). *Journal of Physical Chemistry C* 119 (48): 26828–26839.

105 Cheng, X.-B., Huang, J.-Q., and Zhang, Q. (2017). *Journal of the Electrochemical Society* 165 (1): A6058.

106 Cao, R., Wu, X., Lv, D. et al. (2015). *Advanced Energy Materials* 5 (16): 513–537.

107 Xiong, S., Xie, K., Diao, Y., and Hong, X. (2012). *Electrochimica Acta* 83: 78–86.

108 Zhang, L., Ling, M., Feng, J. et al. (2018). *Energy Storage Materials* 11: 24–29.

109 Cha, E., Patel, M.D., Park, J. et al. (2018). *Nature Nanotechnology* 13 (4): 337–344.

110 Liu, Y., Lin, D., Liang, Z. et al. (2016). *Nature Communications* 7 (1): 1–9.

111 Lin, Z., Liu, Z., Fu, W. et al. (2013). *Advanced Functional Materials* 23 (8): 1064–1069.

112 Akhtar, N., Sun, X., Akram, M.Y. et al. (2021). *Journal of Energy Chemistry* 52: 310–317.

113 Kzlaslan, A., Etinkaya, T., and Akbulut, H. (2020). *Advanced Materials Interfaces* 7 (20): 2001020.

114 Xiong, C., Ren, Y.X., Jiang, H.R. et al. (2019). *Journal of Energy Storage* 26: 101006.

115 Xu, R., Zhang, X.Q., Cheng, X.B. et al. (2018). *Advanced Functional Materials* 28 (8): 1705838.

116 Zhang, X., Wang, W., Wang, A. et al. (2014). *Journal of Materials Chemistry A* 2 (30): 11660–11665.

117 Eftekhari, A. (2017). *Sustainable Energy & Fuels* 1 (1): 14–29.

118 Liu, Y., Wang, J., Xu, Y. et al. (2014). *Journal of Materials Chemistry A* 2 (31): 12201–12207.

119 Koketsu, T., Paul, B., Wu, C. et al. (2016). *Journal of Applied Electrochemistry* 46 (6): 627–633.

120 Chen, Z., Zhao, Y., Mo, F. et al. (2020). *Small Structures* 1 (2): 2000005.

121 Abouimrane, A., Dambournet, D., Chapman, K.W., and Chupas, P.J. (2012). *Journal of the American Chemical Society* 134 (10): 4505–4508.

122 Cui, Y., Abouimrane, A., Sun, C.J. et al. (2014). *Chemical Communications* 50 (42): 5576–5579.

123 Zhou, X., Gao, P., Sun, S. et al. (2015). *Chemistry of Materials* 27 (19): 6730–6736.

124 Park, S., Park, J.S., and Kang, Y.C. (2018). *Journal of Materials Chemistry A* 6 (3): 1028–1036.

125 Li, X., Liang, J., Hou, Z. et al. (2015). *Advanced Functional Materials* 25 (32): 5229–5238.

126 Luo, C., Xu, Y., Zhu, Y. et al. (2013). *ACS Nano* 7 (9): 8003–8010.

127 Cui, Y., Abouimrane, A., Lu, J. et al. (2013). *Journal of the American Chemical Society* 135 (21): 8047–8056.

128 Zeng, L.C., Li, W.H., Jiang, Y., and Yu, Y. (2017). *Rare Metals* 36 (5): 1–26.

129 Jin, J., Tian, X., Srikanth, N. et al. (2017). *Journal of Materials Chemistry A* 5 (21): 10110–10126.

130 Ran, F. and Chen, S.W. (2019). *Advanced Nanomaterials for Electrochemical-Based Energy Conversion and Storage*, 69–114. Elsevier Inc.

131 Patil, A.M., Kumbhar, V.S., Chodankar, N.R. et al. (2016). *Journal of Colloid and Interface Science* 469: 257–262.

132 Liu, L., Hou, Y., Wu, X. et al. (2013). *Chemical Communications* 49 (98): 11515–11517.

133 Lee, S., Lee, H., Ha, N. et al. (2020). *Advanced Functional Materials* 30 (19): 2000028.

134 Xin, S., Yu, L., You, Y. et al. (2016). *Nano Letters* 16: 4560–4568.

135 Zeng, L., Zeng, W., Jiang, Y. et al. (2015). *Advanced Energy Materials* 5 (4): 1401377.

136 He, J., Chen, Y., Lv, W. et al. (2016). *ACS Energy Letters* 1 (1): 16–20.

137 Han, K., Liu, Z., Ye, H., and Dai, F. (2014). *Journal of Power Sources* 263: 85–89.

138 Kai, H., Zhao, L., Shen, J. et al. (2015). *Advanced Functional Materials* 25 (3): 455–463.

139 Lee, J.T., Kim, H., Oschatz, M. et al. (2015). *Advanced Energy Materials* 5 (1): 1–7.

140 Jiang, Y., Ma, X., Feng, J., and Xiong, S. (2015). *Journal of Materials Chemistry A* 3 (8): 4539–4546.

141 Choi, D.S., Yeom, M.S., Kim, Y.-T. et al. (2018). *Inorganic Chemistry* 57 (4): 2149–2156.

142 He, J., Lv, W., Chen, Y. et al. (2017). *Journal of Power Sources* 363: 103–109.

143 Tian, H., Tian, H., Wang, S. et al. (2020). *Nature Communications* 11 (1): 1–12.

144 Hu, J., Ren, Y., and Zhang, L. (2020). *Journal of Power Sources* 455: 227955.

145 Zhang, J., Li, Z., and Lou, X.W. (2017). *Angewandte Chemie International Edition* 56 (45): 14107–14112.

146 Xu, H., Chen, G., Jin, R. et al. (2014). *RSC Advances* 4 (17): 8922–8929.

147 Wu, F., Lee, J.T., Xiao, Y., and Yushin, G. (2016). *Nano Energy* 27: 238–246.

148 Bachman, J.C., Muy, S., Grimaud, A. et al. (2016). *Chemical Reviews* 116 (1): 140–162.

149 Cheng, Z., Pan, H., Zhong, H. et al. (2018). *Advanced Functional Materials* 28 (38): 1707597.

150 Li, X., Liang, J., Luo, J. et al. (2019). *Advanced Materials* 31 (17): 1808100.
151 Zhang, Q., Liu, K., Ding, F., and Liu, X. (2017). *Nano Research* 10 (12): 4139–4174.
152 Xu, L., Tang, S., Cheng, Y. et al. (2018). *Joule* 2 (10): 1991–2015.
153 Lee, J.T., Kim, H., Nitta, N. et al. (2014). *Journal of Materials Chemistry A* 2 (44): 18898–18905.
154 Wang, W.P., Zhang, J., Yin, Y.X. et al. (2020). *Advanced Materials* 32 (23): 2000302.
155 Zhang, Y., Manaig, D., Freschi, D.J., and Liu, J. (2021). *Energy Storage Materials* 40: 166–188.
156 Zhang, X., Jiao, S., Tu, J. et al. (2019). *Energy & Environmental Science* 12 (6): 1918–1927.
157 Zhang, J., Yin, Y.X., You, Y. et al. (2014). *Energy Technology* 2: 757–762.
158 Zhang, Y., Lu, W., Zhao, P. et al. (2021). *Electrochimica Acta* 388: 138621.
159 Zhang, Y., Lu, W., Zhao, P. et al. (2021). *Carbon* 173: 11–21.
160 He, J., Chen, Y., Lv, W. et al. (2016). *ACS Nano* 10 (9): 8837–8842.
161 Xu, J., Xin, S., Liu, J.W. et al. (2016). *Advanced Functional Materials* 26 (21): 3580–3588.
162 Sun, F., Zhang, B., Tang, H. et al. (2018). *Journal of Materials Chemistry A* 6 (21): 10104–10110.
163 Li, S., Han, Z., Hu, W. et al. (2019). *Nano Energy* 60: 153–161.
164 Ding, N., Chen, S.F., Geng, D.S. et al. (2015). *Advanced Energy Materials* 5 (8): 1401999.
165 He, J., Lv, W., Chen, Y. et al. (2017). *ACS Nano* 11 (8): 8144–8152.
166 Yin, H., Yu, X.-X., Yu, Y.-W. et al. (2018). *Electrochimica Acta* 282: 870–876.
167 Huang, D., Li, S., Xiao, X. et al. (2017). *Journal of Power Sources* 371: 48–54.
168 Li, Y., Zhang, Y., Xu, Q. et al. (2019). *ChemSusChem* 12 (6): 1196–1202.
169 Lu, G., Ye, C., Li, W. et al. (2021). *Frontiers in Chemistry* 9: 377.
170 Zhang, S.S. (2013). *Frontiers in Energy Research* 1: 10.
171 Yang, H., Chen, J., Yang, J., and Wang, J. (2020). *Angewandte Chemie* 132 (19): 7374–7386.
172 Chen, S. and Zhang, J. (2020). *Dalton Transactions* 49 (29): 9929–9934.
173 Xing, M., Zhao, Z., Zhang, Y. et al. (2020). *Materials Today Energy* 12: 100534.
174 Xie, C., Liu, Y., Lu, W. et al. (2019). *Energy & Environmental Science* 12 (6): 1834–1839.
175 Ma, J., Liu, M., He, Y., and Zhang, J. (2021). *Angewandte Chemie* 133 (23): 12744–12755.
176 Skarstad, P.M. and Schmidt, C.L. (1993). *Journal of Power Sources* 43: 111–118.
177 Wang, Y., Sun, Q., Zhao, Q. et al. (2011). *Energy & Environmental Science* 4 (10): 3947–3950.
178 Li, K., Lin, B., Li, Q. et al. (2017). *ACS Applied Materials & Interfaces* 9 (24): 20508–20518.
179 Zhao, Q., Lu, Y., Zhu, Z. et al. (2015). *Nano Letters* 15 (9): 5982–5987.
180 Zhang, Q., Wu, Z., Liu, F. et al. (2017). *Journal of Materials Chemistry A* 5 (29): 15235–15242.

181 Su, Z., Ling, H.Y., Li, M. et al. (2020). *Carbon Energy* 2 (2): 265–275.
182 Zhang, Q., Zeng, Y.-H., Ye, S.-H., and Liu, S. (2020). *Journal of Power Sources* 463: 228212.
183 Su, Z., Wei, Z., Lai, C. et al. (2018). *Energy Storage Materials* 14: 129–135.
184 Li, K., Chen, S., Chen, S. et al. (2019). *Nano Research* 12 (3): 549–555.
185 Sun, C., Shi, X., Zhang, Y. et al. (2020). *ACS Nano* 14 (1): 1176–1184.
186 Wang, F., Liu, Z., Yang, C. et al. (2020). *Advanced Materials* 32 (4): 1905361.
187 Fang, C., Wang, X., and Meng, Y.S. (2019). *Trends in Chemistry* 1 (2): 152–158.
188 Zhang, X.Q., Cheng, X.B., and Zhang, Q. (2018). *Advanced Materials Interfaces* 5 (2): 1701097.
189 Li, K., Hu, Z., Ma, J. et al. (2019). *Advanced Materials* 31 (33): 1902399.
190 Lai, Q., Zhang, H., Li, X. et al. (2013). *Journal of Power Sources* 235: 1–4.
191 Chang, Z., Wang, X., Yang, Y. et al. (2014). *Journal of Materials Chemistry A* 2 (45): 19444–19450.
192 Xi, X., Li, X., Wang, C. et al. (2017). *Journal of Energy Chemistry* 26 (4): 639–646.
193 Etacheri, V., Marom, R., Elazari, R. et al. (2011). *Energy & Environmental Science* 4 (9): 3243–3262.
194 Li, H. (2019). *Joule* 3 (4): 911–914.
195 Li, B., Wang, Y., Jiang, N. et al. (2020). *Nano Energy* 72: 104727.
196 Wu, W., Wang, M., Wang, J. et al. (2020). *Nano Energy* 74: 104867.
197 Hewavitharana, I.K., Ding, Y., Ng, K.S., and Deng, D. (2021). *Chemical Engineering Science* 236: 116480.
198 Jung, S.-K., Kim, H., Cho, M.G. et al. (2017). *Nature Energy* 2 (2): 1–9.
199 Paul, P.P., McShane, E.J., Colclasure, A.M. et al. (2021). *Advanced Energy Materials* 11 (17): 2100372.
200 Lin, D., Liu, Y., and Cui, Y. (2017). *Nature Nanotechnology* 12 (3): 194.
201 Jie, Y., Ren, X., Cao, R. et al. (2020). *Advanced Functional Materials* 30 (25): 1910777.
202 Qian, J., Henderson, W.A., Xu, W. et al. (2015). *Nature Communications* 6 (1): 1–9.
203 Kamaya, N., Homma, K., Yamakawa, Y. et al. (2011). *Nature Materials* 10 (9): 682–686.
204 Li, N.W., Yin, Y.X., Yang, C.P., and Guo, Y.G. (2016). *Advanced Materials* 28 (9): 1853–1858.
205 Lin, D., Liu, Y., Liang, Z. et al. (2016). *Nature Nanotechnology* 11 (7): 626–632.
206 Cheng, X.-B., Zhao, C.-Z., Yao, Y.-X. et al. (2019). *Chem* 5 (1): 74–96.
207 Zhao, W., Ji, Y., Zhang, Z. et al. (2017). *Current Opinion in Electrochemistry* 6 (1): 84–91.
208 Patten, H.E. and Mott, W.R. (2002). *The Journal of Physical Chemistry* 8 (3): 153–195.
209 Meibuhr, S.G. (1971). *Journal of the Electrochemical Society* 118 (8): 1320.
210 Whittingham, M.S. and Gamble, F.R. Jr., (1975). *Materials Research Bulletin* 10 (5): 363–371.

211 Gachot, G., Grugeon, S., Armand, M. et al. (2008). *Journal of Power Sources* 178 (1): 409–421.
212 Miao, R., Yang, J., Xu, Z. et al. (2016). *Scientific Reports* 6 (1): 1–9.
213 Zhang, H., Eshetu, G.G., Judez, X. et al. (2018). *Angewandte Chemie International Edition* 57 (46): 15002–15027.
214 Li, F., He, J., Liu, J. et al. (2020). *Angewandte Chemie International Edition* 60 (12): 6600–6608.
215 Qi, S., He, J., Liu, J. et al. (2021). *Advanced Functional Materials* 31 (11): 2009013.
216 Amine, R., Liu, J., Acznik, I. et al. (2020). *Advanced Energy Materials* 10 (25): 2000901.
217 Nilsson, V., Kotronia, A., Lacey, M. et al. (2019). *ACS Applied Energy Materials* 3 (1): 200–207.
218 Ren, X., Chen, S., Lee, H. et al. (2018). *Chem* 4 (8): 1877–1892.
219 Cao, X., Xu, Y., Zhang, L. et al. (2019). *ACS Energy Letters* 4 (10): 2529–2534.
220 Jiao, S., Ren, X., Cao, R. et al. (2018). *Nature Energy* 3 (9): 739–746.
221 Li, Q., Jiao, S., Luo, L. et al. (2017). *ACS Applied Materials & Interfaces* 9 (22): 18826–18835.